Kathryn's Wheel: a spectacular galaxy collision discovered in the Galactic neighbourhood[★]

Quentin A. Parker,[1,2]† Albert A. Zijlstra,[3]† Milorad Stupar,[4] Michelle Cluver,[5] David J. Frew,[1] George Bendo[3] and Ivan Bojičić[1]

[1]*Department of Physics, Chong Yuet Ming Physics Building, The University of Hong Kong, Hong Kong*
[2]*Australian Astronomical Observatory, PO Box 915, North Ryde, NSW 1670, Australia*
[3]*Jodrell Bank centre for Astrophysics, School of Physics and Astronomy, University of Manchester, Oxford Road, Manchester M13 9PL, UK*
[4]*University of Western Sydney, Locked Bag 1797, Penrith South, DC, NSW 1797, Australia*
[5]*University of the Western Cape, Robert Sobukwe Road, Bellville 7535, South Africa*

ABSTRACT

We report the discovery of the closest collisional ring galaxy to the Milky Way. Such rare systems occur due to 'bulls-eye' encounters between two reasonably matched galaxies. The recessional velocity of about 840 km s^{-1} is low enough that it was detected in the Anglo-Australian Observatory/UK Schmidt Telescope Survey for Galactic Hα emission. The distance is only ∼10 Mpc and the main galaxy shows a full ring of star-forming knots, 6.1 kpc in diameter surrounding a quiescent disc. The smaller assumed 'bullet' galaxy also shows vigorous star formation. The spectacular nature of the object had been overlooked because of its location in the Galactic plane and proximity to a bright star and even though it is the 60th brightest galaxy in the HI Parkes All Sky Survey (HIPASS) H I survey. The overall system has a physical size of ∼15 kpc, a total mass of $M_* = 6.6 \times 10^9$ M$_\odot$ (stars + H I), a metallicity of [O/H]∼ −0.4, and a star formation rate of 0.2–0.5 M$_\odot$ yr^{-1}, making it a Magellanic-type system. Collisional ring galaxies therefore extend to much lower galaxy masses than commonly assumed. We derive a space density for such systems of 7×10^{-5} Mpc^{-3}, an order of magnitude higher than previously estimated. This space density suggests Kathryn's Wheel is the nearest such system. We present discovery images, CTIO 4-m telescope narrow-band follow-up images and spectroscopy for selected emission components. Given its proximity and modest extinction along the line of sight, this spectacular system provides an ideal target for future high spatial resolution studies of such systems and for direct detection of its stellar populations.

Key words: galaxies: groups: general – galaxies: individual (ESO 179-13) – galaxies: interactions – galaxies: kinematics and dynamics – galaxies: star formation.

1 INTRODUCTION

Among the structures shown by interacting galaxies (Barnes & Hernquist 1992), the so-called collisional ring galaxies (Theys & Spiegel 1976, 1977) are a rare and most distinctive sub-class (Appleton & Struck-Marcell 1996). Collisional ring galaxies occur from an almost head-on collision between a smaller galaxy travelling along the minor axis of a larger galaxy passing through, or close to, its centre (Appleton & Struck-Marcell 1996). The shock wave sweeps up and expels gas from the system, usually leaving a gas-poor galaxy behind (Freeman & de Vaucouleurs 1974).

The pre-eminent example is the Cartwheel galaxy (ESO 350-40; AM 0035-335) at a distance of 124 Mpc. The Cartwheel was discovered by Zwicky (1941), and studied in-depth by Fosbury & Hawarden (1977) and Amram et al. (1998). The Cartwheel shows a spectacular ring of star formation, with interior spokes surrounding the host galaxy. Other well-known collisional systems include Arp 148 (Mayall's Object) at 148 Mpc (Smith 1941; Burbidge, Burbidge & Prendergast 1964; Arp 1966), IC 298 (Arp 147; Gerber, Lamb & Balsara 1992) at 135 Mpc, and AM 0644-741 (ESO 34-11 or the 'Lindsay–Shapley Ring') at 87 Mpc (Lindsay & Shapley 1960; Graham 1974; Arp & Madore 1987). This latter object is often considered to be a typical exemplar of evolved ringed galaxies (e.g. Higdon, Higdon & Rand 2011).

While star-forming events resulting from galactic collisions may be more common than usually thought (e.g. Block et al. 2006),

---

[★]Named after the wife of the second author.
†E-mail: quentinp@hku.hk (QAP); a.zijlstra@manchester.ac.uk (AAZ)

spectacular cartwheel-type galaxies, showing complete rings (but not necessarily with evident spokes), appear to be very rare in volume-limited surveys. The previous nearest example was the Vela Ring galaxy (AM 1006-380 = ESO 316-43), at 72 Mpc (Dennefeld, Lausten & Materne 1979). Partial ring galaxies are more numerous. Probably the nearest in the Madore, Nelson & Petrillo (2009) catalogue is AM 0322-374 at 20 Mpc. UGC 9893, at 11 Mpc (Kennicutt et al. 2008), is also listed as a collisional system, but it lacks a clear ring structure (Gil de Paz, Madore & Pevunova 2003), appearing indistinct in available imagery. Collisional ring galaxy systems can be identified in high-resolution, deep H α imagery where the H II regions of the ring are readily visible. However, H α galaxy surveys such as Gil de Paz et al. (2003), James et al. (2004), and Kennicutt et al. (2008) have not added to the modest number of cartwheel-type galaxies currently known and there are <20 convincing systems, e.g. Marston & Appleton 1995. Brosch et al. (2015) present the most recent detailed work on such systems for an apparently empty ring galaxy system ESO 474 G040 at ∼78 Mpc, thought to have arisen from a recent merger of two disc galaxies.

Collisional rings systems offer an excellent environment to study the evolution of density-wave-induced starbursts (Marston & Appleton 1995; Romano, Mayya & Vorobyov 2008), as well as the dynamic interactions between the individual galaxies (e.g. Smith et al. 2012). A closer example of a collisional ring system would allow its star formation, stellar distribution, and evolution to be studied in detail, spatially, kinematically and chromatically. Here, we present the discovery of a new collisional ring galaxy at a distance of only 10 Mpc. Our paper is organized as follows. In Section 2, we present some background and describe the discovery of the ring around ESO 179-13. In Section 3, we present our follow-up high-resolution imaging and other archival multiwavelength images. Optical spectroscopy is presented in Section 4. Parameters for the system, such as masses and star formation rates (SFR), are provided in Section 5. Section 6 presents our discussion and gives our summary in Section 7.

2 BACKGROUND AND DISCOVERY

2.1 Background

ESO 179-13 is noted as an interacting double galaxy system in SIMBAD, appearing to consist of a near edge-on late-type spiral with another more chaotic system ∼80 arcsec to the northeast. It was first identified by Sersic (1974) and independently re-discovered by Lauberts (1982), Longmore et al. (1982) and Corwin, de Vaucouleurs & de Vaucouleurs (1985). A detailed *B*-band image was published by Laustsen, Madsen & West (1987).

Woudt & Kraan-Korteweg (2001) identify the most prominent galaxy as WKK 7460 (component A hereafter), and WKK 7463 for the secondary (component B). A small, third galaxy is also identified as WKK 7457 to the west of component A (component C). It agrees with our own positional determination to 1 arcsec. The system, centred on component A, is entry 391 in the H α catalogue of Kennicutt et al. (2008), but they do not list integrated H α (+ [N II]) flux or luminosity estimates. Lee et al. (2011), in a related paper, included this system in their Galaxy Evolution Explorer (GALEX) ultraviolet (UV) imaging survey of local volume galaxies with a quoted $B_T = 15$, but no near-UV or far-UV fluxes are quoted. Owing to its proximity to the Galactic plane, the galaxy was not observed by GALEX prior to mission completion (Bianchi 2014).

Component A has been classified as an SB (s) m spiral in the RC3 catalogue (de Vaucouleurs et al. 1991) and similarly classified

as SB (s) dm system ($T = 7.5$) by Buta (1995). These independent classifications treat the system as a distinct, late-type spiral galaxy, albeit in an interaction. It can be best described as a Magellanic dwarf or a Magellanic spiral, similar to the Large Magellanic Cloud (LMC).

A range of heliocentric radial velocities for component A are available in the literature from both optical spectroscopic and H I measurements. The most recent optical results are Strauss et al. (1992) who quote 775 ± 36 km s^{-1}, Di Nella et al. (1997), 750 ± 70 km s^{-1}, and Woudt, Kraan-Korteweg & Fairall (1999), 757 ± 50 km s^{-1}. These are in good agreement so we take an unweighted average of 761 km s^{-1} ($\sigma = 11$ km s^{-1}) for component A.

The earliest H I heliocentric velocities towards the system are 836 ± 5 km s^{-1} by Longmore et al. (1982), 840 ± 20 km s^{-1} by Tully (1988) and 843 ± 9 km s^{-1} by de Vaucouleurs et al. (1991). The Parkes H I 'HIPASS' Multibeam receiver programme gives 843 ± 5 km s^{-1} (HIPASS catalogue; Meyer et al. 2004), where it is noted as the 60th brightest in terms of integrated flux density (Koribalski et al. 2004). A deeper, pointed Parkes observation was obtained by Schröder, Kraan-Korteweg & Henning (2009). They give parameters for component A, but note that a contribution from component B is likely. Their heliocentric H I radial velocity is 842 km s^{-1} from the H I profile mid-point, with a velocity width of 222 km s^{-1} at 20 per cent of peak. The integrated H I flux density is 113.8 ± 3.7 Jy km s^{-1}, in good agreement with the HIPASS value of 100. All the H I velocities are consistent within small errors. These values include the combined contribution from all the gas in the full system. We adopt 842 ± 5 km s^{-1} for the combined H I system velocity.

Kennicutt et al. (2008) give a distance of 9 Mpc based on a Virgocentric flow model distance. We adopt a slightly further distance of 10.0 ±1.0 Mpc, based on Kennicutt et al. (2008), but scaling from a Hubble constant H$_0$ of 75 to 68 km s^{-1} Mpc^{-1} due to the latest *Wilkinson Microwave Anisotropy Probe* (Hinshaw et al. 2013) and *Planck* results (Ade et al. 2014). At this distance, 1 arcsec equates to 48.5 pc. Woudt & Kraan-Korteweg (2001) gives a modest colour excess of $E(B-V) = 0.25$ mag in the surrounding field, giving $A_V = 0.78$ mag, while Schlafly & Finkbeiner (2011) give $A_V = 0.75$ mag for Galactic extinction in this general direction, which we adopt hereafter. We will also use $A_{H\alpha} = 0.61$ mag based on the reddening law from Howarth (1983).

Apart from the basic information above, the system has been little studied because of its location in a crowded, low-latitude area near the Galactic plane ($|b| = -8°$) and proximity to the bright, 7.7 mag A0 IV star, HD 150915, located 72 arcsec due south. There are actually two bright stars here, but only HD 150915 is listed in SIMBAD. The second star is ∼10 arcsec north of HD 150915 and ∼2 mag fainter. It was undoubtedly blended with HD 150915 in the original photographic imagery.

2.2 Discovery of the ring

The low heliocentric velocity meant the system was discovered as a strong H α emitter in the Anglo-Australian Observatory (AAO) / UK Schmidt Telescope (UKST) SuperCOSMOS H α survey of the Southern Galactic Plane (SHS; Parker et al. 2005) during searches for Galactic planetary nebulae (Parker et al. 2006). The bandpass of the survey filter (Parker & Bland-Hawthorn 1998) includes all velocities of Galactic gas and emission from extragalactic objects out to the Virgo and Fornax galaxy clusters at ∼1200 km s^{-1}.

Fig. 1 shows the 4 × 4 arcmin discovery images from the SHS survey data centred on the system. From left to right there is the
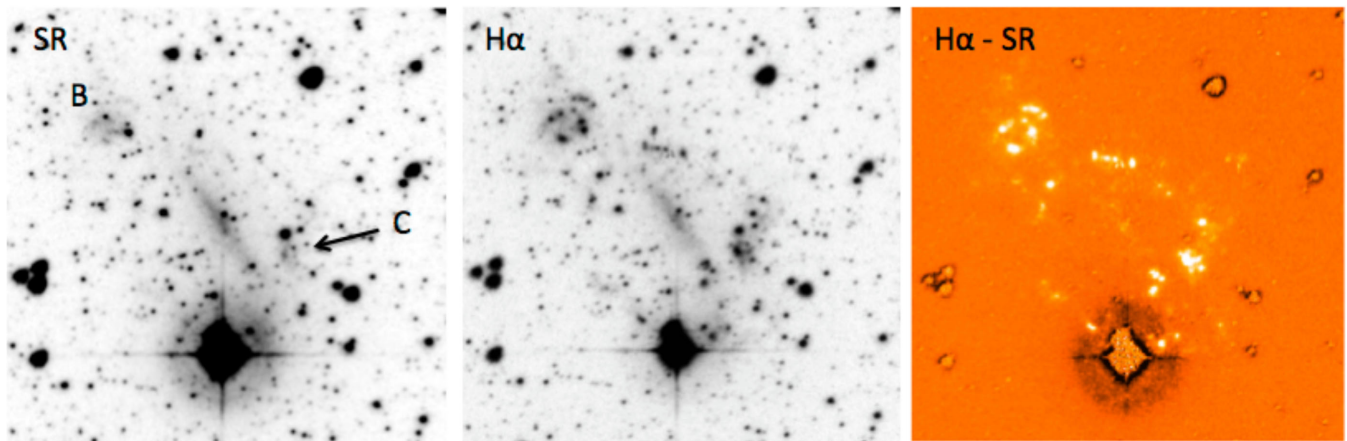
Figure 1. Left-hand panel: The 4 × 4 arcmin SHS broad-band short-red 'SR' image centred on component A at $16^h47^m19\overset{s}{.}7$, $-57°26'31''$ (J2000). North is top and east left. Mid panel: The matching H α image. Right-hand panel: The continuum-subtracted image obtained by taking the SR from the SHS H α (+ [N II]) image scaled at 99.5 per cent. North is at the top and east to the left. Component B is labelled to the north-east and component C is indicated with an arrow.

H α image, the matching broad-band short-red 'SR' image and the image obtained by taking the SR image from the H α image (effectively a continuum-subtracted image). Component A is at the centre. Component B is labelled to the north-east, while the smaller compact component C is indicated with an arrow.

The SHS continuum-subtracted image reveals a spectacular ring of emission knots not obvious, without context, even in the H α image, while the main component A galaxy has almost disappeared. The ring is approximately (but not perfectly) centred on component A. Surprisingly, given its previous spiral morphological classification, component A does not show up well in the SHS continuum-subtracted image and appears to show little star formation. This indicates that along with its apparently highly elongated nature (so not an elliptical) it is has been largely stripped of gas. The smaller, more irregular galaxy (component B), which we assume is the bullet that impacted the target galaxy, component A, shows extensive, clumpy H α emission. A third, faint compact system (component C) is seen 38 arcsec to the west of component A, identified as WKK 7457. This object is clear in the broad-band *B*-, *R*-, and *I*-band SuperCOSMOS images and is also undergoing star-formation.

The strong H I detection noted earlier indicates that a significant, neutral H I component still remains within the overall system environment. The lack of much star formation in component A suggests that most of this H I may be located outside of its inner disc.

3 FOLLOW-UP IMAGING AND MULTIWAVELENGTH COMPARISONS

Discovery of this collisional ring system led us first to investigate and compile existing multiwavelength data from the archives. We then obtained deeper, higher resolution imaging and spectroscopy of the major emission components (see below), to provide estimates of some key physical parameters for this system.

3.1 CTIO 4-m-telescope imaging

High-resolution imagery at the Blanco 4-m telescope at CTIO was obtained in 2008 June using the wide field mosaic camera. We used five filters: *V*-band, Hα, H α off-band (80Å redward of H α), [O III] , and a (wider) [O III] off-band filter centred at 5300Å. The field of

view is 30 arcmin on a side and the plate scale 0.26 arcsec px^{-1}. The seeing measured from the data frames was typically 1.2 arcsec. Exposures were 5 min for the emission-line and off-band filters, and 60 s for the *V*-band filter. The airmass during the exposures averaged 1.3. To subtract the continuum, the H α off-band image was scaled down by a factor of 0.88, and the [O III] off-band by a factor of 0.14, to compensate for the filter widths. These factors were established by minimizing residuals for a set of selected field stars. For [O III] that works very well and results are in good agreement with the filter curve. For H α this can be an issue if the chosen stars have H α in absorption. This does not appear to be the case for the field stars chosen which provide a consistent scale-factor to ~2 per cent. It is best to minimize stellar residuals rather than filter curves as stars are a more important contribution to the continuum than bound-free emission from H I regions.

A montage of these CTIO images is shown in Fig. 2. They reveal the distribution and variety of the emission structures as well as data for quantitative flux estimates. From these deeper, higher resolution CTIO H α and [O III] continuum-subtracted images, the distribution of ionized gas is seen to be far more complex than is evident from the SHS discovery data.

The leftmost panel is a 3 × 3 arcmin CTIO H α image with the off-band frame subtracted. We avoid the bright star to the south where CCD blooming is serious. Emission associated with component C and at the southern tip of component A's disc previously gave the impression of a circular ring in the SHS as the bright star obscured emission further south. The higher resolution CTIO data reveals an elliptical emission ring with a major-axis diameter of 127 arcsec (~6.2 kpc). The inscribed oval was positioned to fit the prominent emission now seen to extend further south. The ellipse is not centred on component A, but at $16^h47^m19\overset{s}{.}5$, $-57°26'44''$ (J2000), ~13 arcsec (or ~0.6 kpc) south-south-east. Some low-level H α emission is now seen across component A, surrounding component B and with faint, localized emission features and blobs around the entire system. An interesting feature is the elongated nature of some of these emission knots in a north-east direction from A to B. The main [O III] emission features follow the equivalent H α structures though at typically a third to a half of their native integrated pixel intensities.

The mid panel is the matching CTIO continuum-subtracted [O III] image (narrow on and off-band [O III] images used). Both

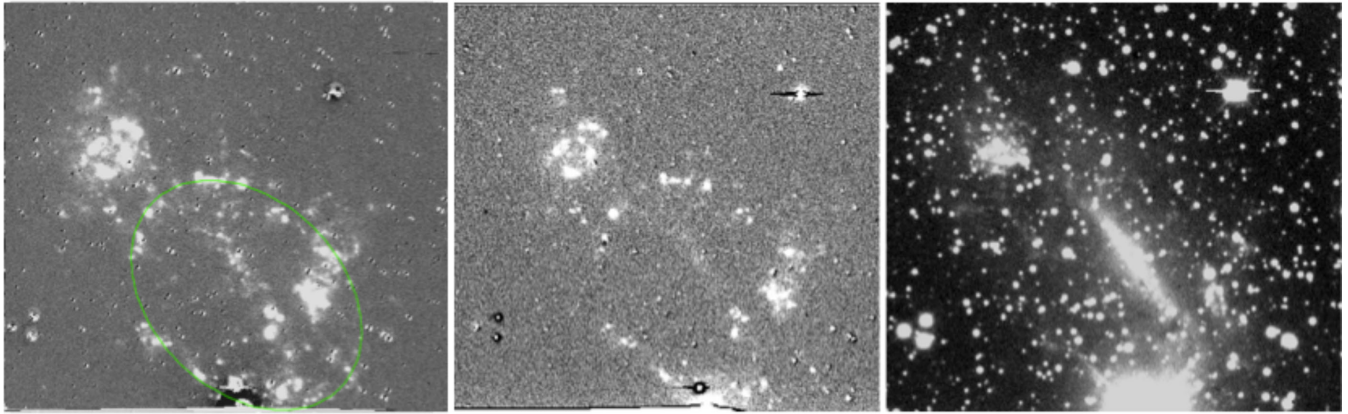**Figure 2.** Selected 3 × 3 arcmin regions from the CTIO 4-m imaging centred at $16^h47^m21^s, -57°26'03''$ (J2000). Left-hand panel: the CTIO continuum-subtracted H α. The green oval has a major axis diameter of 127 arcsec (~6.2 kpc) and a minor axis of 91 arcsec (~4.4 kpc). Mid panel: matching CTIO continuum-subtracted [O III] image. Both these images are at 90 per cent scaling to better reveal the emission otherwise the 7.7th magnitude star dominates. Right-hand panel: CTIO [O III] off-band image. This represents the *V*-band starlight without any [O III] and Hβ emission line contribution. Dust lanes can be clearly seen at the southern tip of component A. The more diffusely distributed starlight can also be seen in and around components A and B.

these images are presented at 90 per cent linear scaling to reveal the full extent of the emission (this sets the upper and lower limits based on the 90 per cent pixel intensity level where a histogram of the data is created and the limits are set to display the percentage about the mean value). With full pixel range, saturated pixels from the 7.7th magnitude star HD 150915 would prevent detail being seen. Low-level diffuse [O III] flux is seen for component A, but it is not conspicuous. This shows it has almost been completely cancelled out indicating component A is mostly composed of normal starlight.

The right-hand panel is the off-band [O III] filter image (5300Å) that effectively represents the *V*-band starlight without the [O III] +Hβ emission line contribution. This shows dust lanes along and at the south-west extremity of the disc, concentrated starlight from components A, B, and C and an envelope of diffuse starlight around the entire system. This 'common envelope' was already noted by Laustsen et al. (1987) from old *B*-band photographic data taken with the ESO 3.6-m telescope in the 1980s. This raises an interesting question and also a possible explanation for why the apparent axial ratios of the highly elongated component A differs so much from the surrounding oval ring. Currently known collisional ring systems with low-impact parameter have axial ratios that are broadly similar to that of the target galaxy. Such arrangements are a natural consequence of the copious gas and interstellar medium being swept up and compressed by the resultant density wave having a similar radial (and perhaps also vertical) distribution as the target galaxy stellar content. This does not appear to be the case here unless what we are actually seeing is the residual, less-inclined bar of a more face-on disc system that extends out to the entire ring and whose presence can still be seen in the low-level diffuse starlight refereed to earlier. If component A is not a residual bar but a distinct late-type disc galaxy (as commonly assumed) stripped of gas, then the gas distribution could have become less flattened somehow. Alternatively the original target galaxy could have been stretched out along the direction of the impact towards component B before, during, or even after the bulls-eye collision occurred. Though component B is only 13 per cent of the mass (in stars) of component A, these effects could have been strengthened due to the low 'Magellanic'-type masses of the system as a whole.

Finally, Fig. 3 is a composite Red, Green, Blue (RGB) CTIO image displaying the system's spectacular nature. The red channel

is H α, the green [O III] and the blue broad-band V. Component A is mostly starlight with dust lanes evident in this higher resolution data. The few small H II knots appear red, likely due to dust extinction within the disc.

Based on the SHS data, literature data, and our new CTIO images, Table 1 presents some key parameters for galaxy components A, B, and C, including the central position of the best-fitting ellipse to the main emission ring. The position for component A is tied to the 2MASS (Skrutskie et al. 2006) near-infrared (NIR) imagery and astrometry. The positions refer to the centre of each assumed galaxy. The centre of component A is derived from the dominant starlight in the *R* band. The separation between the centres of components A and B is ~80 arcsec. Using the distance of 10 Mpc gives a projected separation between them of 3.9 kpc.

Component A has a major-axis of ~86 arcsec (4.2 kpc) measured to the outer edge in the stellar continuum from off-band [O III] and *V*-band CTIO images, where a decline in the background is seen before the star-forming ring is encountered. When checked against the broad-band *R*, *I* and 2MASS images when autocut at the 90 per cent pixel intensity level, the disc appears to extend only to 70–80 arcsec. At low isophotal thresholds, starlight extends out to the star-forming ring both along the major and minor axes. Component B has a major axis of ~33 arcsec (1.6 kpc) determined in the same way. The strongest H α emission in B is also in an oval structure of nucleated knots ~32 arcsec across. This is in excellent agreement with the value estimated from the concentrated starlight. Starlight internal to this emission oval is clear in Fig. 3 and B may extend to 70 arcsec (~3.4 kpc) in low level, isolated clumps of star formation and diffuse starlight.

The overall system envelope, including all assumed associated broad and narrow band emission and diffuse starlight as seen across the region in the right-hand panel of Fig. 2, has a major diameter of 318 arcsec and a minor axis of 198 arcsec, giving a total system size of ~15.4 × 9.6 kpc.

3.2 Near and mid infrared imaging

The 2MASS colour combined *J*-, *H*-, and K_s-band image (as red, green, blue) is presented in the left-hand panel of Fig. 4. The old stellar population of component A is clear in the NIR and seen to be well separated from component B (surrounded by a blue
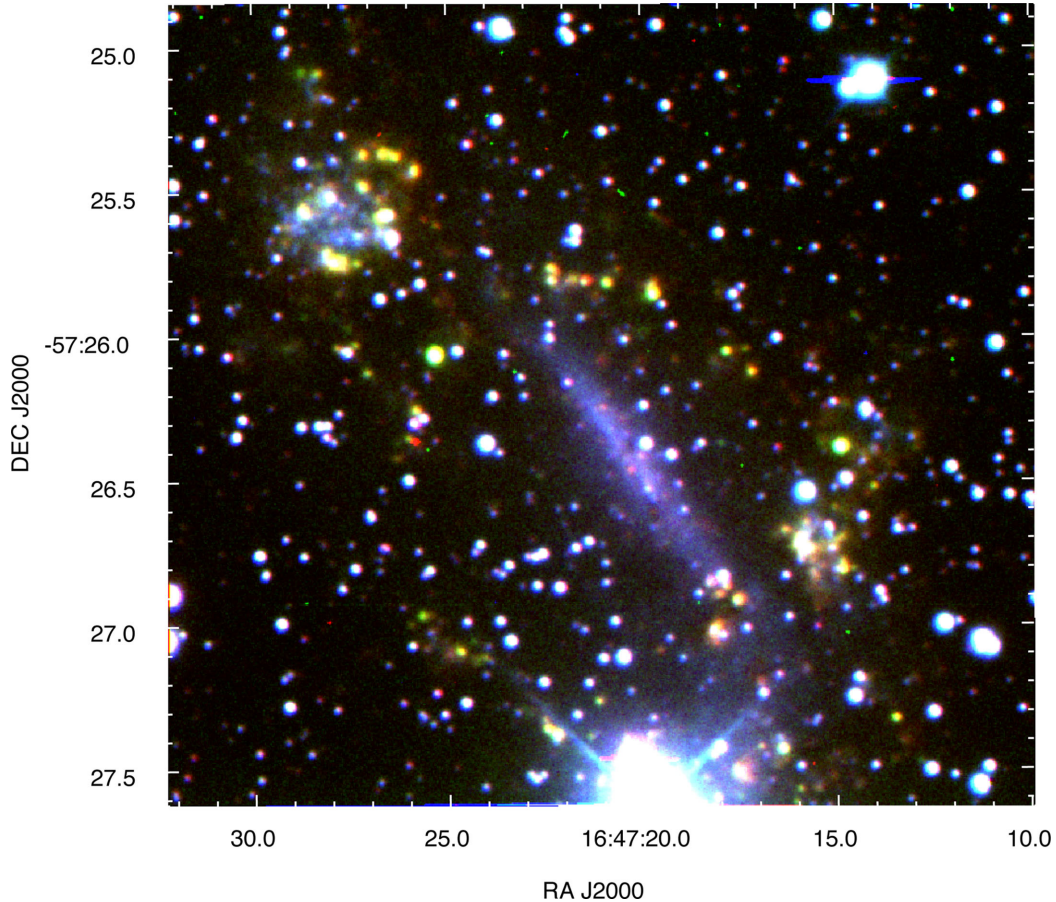
Figure 3. A colour composite RGB CTIO image displaying the system's spectacular nature. The red channel is H α, the green [O III] and the blue is broad-band V. Component A is mostly normal starlight with dust lanes also evident in this higher resolution data as well as the likely effect of dust on the small H II knots along the disc where they appear reddish or orange at the southern edge.

Table 1. Fundamental parameters of Kathryn's wheel. Component A is the main system near the ring's centre. Component B is the smaller system directly to the north-east. Component C is projected internal to the ring to the south-west. It also has a concentrated stellar component so is also considered a distinct galaxy. The oval ring completely encompasses component A.

Parameter	A	B	C	Ring	A-B separation
RA (J2000)	16:47:19.7	16:47:27.8	16:47:15.5	16:47:21.1	–
Dec. (J2000)	−57:26:31	−57:25:35	−57:26:44	−57:26:36	–
Size (arcsec)	86	33	16	127	80
Size (kpc)	4.2	1.6	0.8	6.2	3.9

circle) located towards the top left of the image, indicating it is a distinct galaxy. Component C (surrounded by a blue circle to the right of Component A) is also just visible. Each NIR component is scaled at the 95 per cent level in the linear combination. A low-level background is also apparent which needs to be included in any overall NIR magnitude estimates. The NIR magnitude differences between components A and B is $\Delta J \sim \Delta K \sim 3.1$. There is also only a mild colour term for each main component with $J - K \sim 0.3$ for component A and -0.05 ± 0.05 for component B.

The *Wide-field Infrared Survey Explorer*, *WISE* (Wright et al. 2010) surveyed the entire sky at 3.4, 4.6, 12, and 22 µm (bands named *W*1 to *W*4). The right-hand panel of Fig. 4 shows the *WISE* 'hi-res' mid-IR (MIR) combined colour image of bands *W*4, *W*3, and *W*2 (as blue, green, red) from drizzled data. The *WISE* mission provides 'Atlas' images, co-added from individual frames, through

the web server hosted at IPAC.[1] The images have beam sizes of 8.1, 8.8, 11.0, and 17.5 arcsec for the *W*1, *W*2, *W*3, and *W*4 bands, respectively.

To regain valuable spatial resolution, we made use of the Image Co-addition with Optional Resolution Enhancement[2] (ICORE) software (Masci 2013) which exploits the stable point spread function of *WISE*. The 'drizzled' co-added images make use of a variable pixel linear reconstruction (VPLR) technique employing a 'Tophat' point response function kernel. The 'HiRes' images additionally use a maximum correlation method) technique as outlined in Masci & Fowler (2009). The drizzle images have a resolution of 5.9, 6.5,
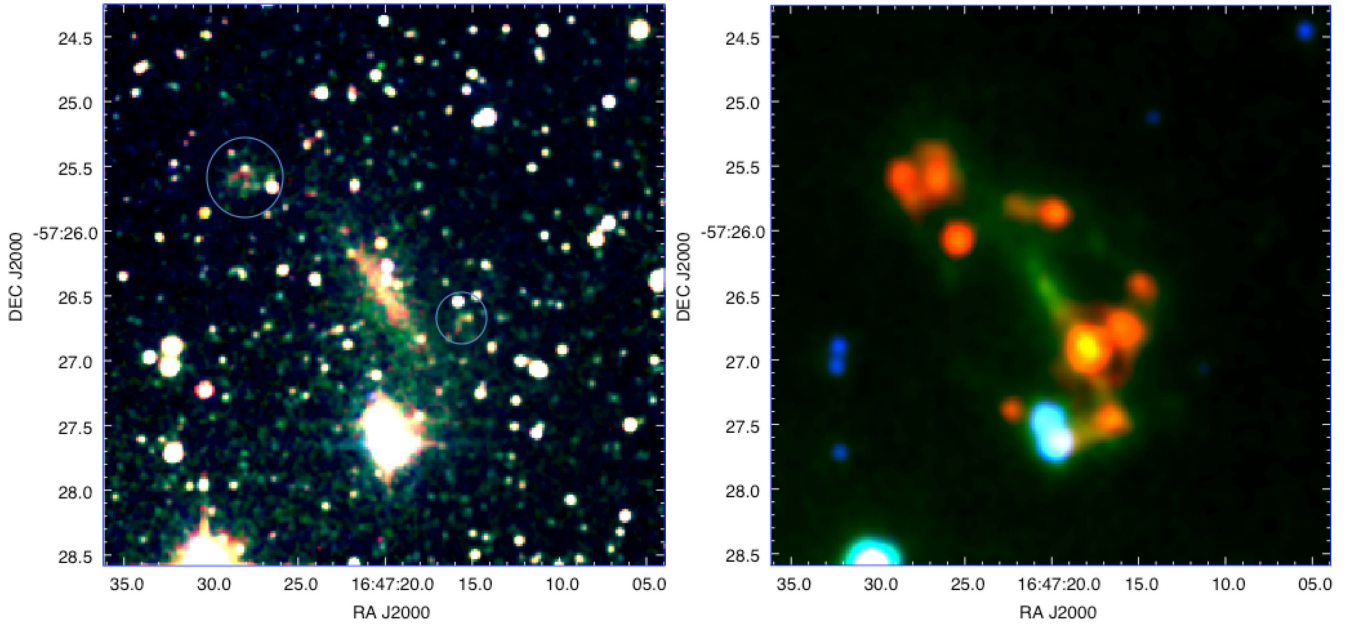
Figure 4. Left: a 4×4 arcmin colour mosaic of the 2MASS *J*-, *H*-, and *K*$_s$-band data of the system (as blue, green, red). North is top and east left. Component A at the centre is clearly visible revealing the old residual stellar population. Component B (surrounded by a blue circle) is obvious towards the top left of the image, indicating it is a distinct galaxy. Component C (surrounded by a blue circle to the right of component A) is also just visible. Right: the equivalent 'hi-res' *WISE* mid-IR combined colour image of bands 4, 3, and 2 (as blue, green, red) from drizzled data. Component A is strong in W3 centred at 12 μm. The emission is likely thermal from diffuse interstellar dust and PAHs. Several knots in oval ring are particularly bright in W4. This is related to hot (∼100 K) dust continuum emission from ongoing star formation in these regions.
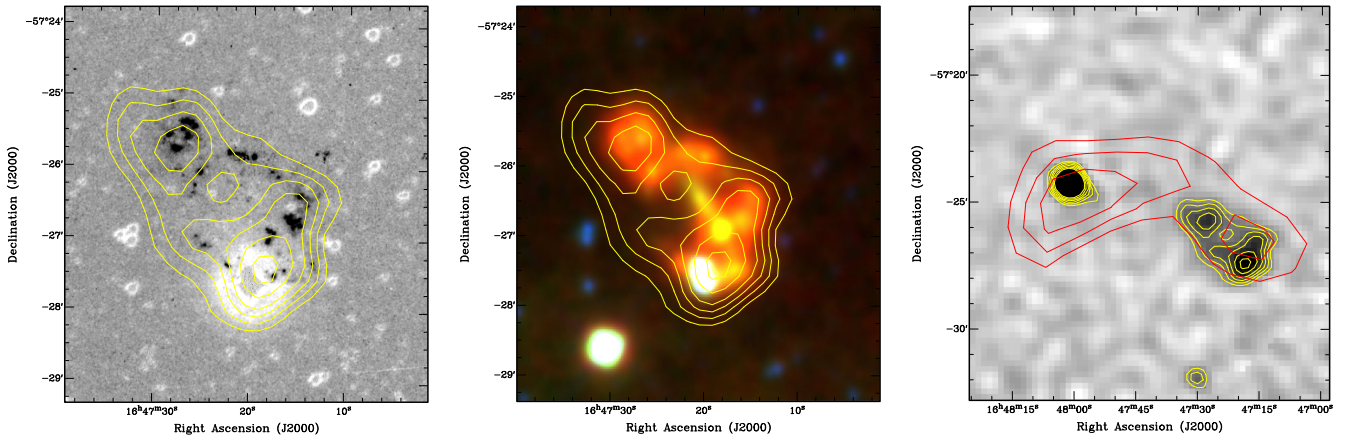

Figure 5. Left and middle: SHS/H α quotient image and *WISE* RGB colour composite, respectively, overlaid with contours from the MGPS2 radio image at 3, 5, 7, 9, 12, and 15 × σ$_{mgps2}$ (σ$_{mgps2}$ = 1.1 mJy beam^{-1}). These panels are 5 × 6 arcmin in size. Right: MGPS2 total intensity image overlaid with radio contours from MGPS2 (same as in previous images) and from PMN at 3, 4, and 5 × σ$_{pmn}$ (σ$_{pmn}$ = 8 mJy beam^{-1}). Here the image is 13 × 18 arcmin. North-east is to the left in all panels.

7.0, and 12.4 arcsec for bands *W*1 to *W*4, respectively (Jarrett et al. 2012). Component A is prominent in *W*3 centred at 12 μm but with sharp cut-on and cut-offs at 7 and 17 μm. This is likely indicative of thermal emission from diffuse interstellar dust and polycyclic aromatic hydrocarbons (PAHs) in the disc. The presence of clear dust lanes visible in the CTIO *V*-band image along component A supports this and shows that component A has not been entirely stripped of its gaseous component.

3.3 Existing radio data

In the radio regime, the system is detected in the second epoch Molonglo Galactic Plane Survey (MGPS2; Murphy et al. 2007). The

MGPS2 was performed with the Molonglo Observatory Synthesis Telescope at a frequency of 843 MHz and with a restoring beam of ∼45 arcsec. In MGPS2, the system is resolved into two main components catalogued as MGPS J164718−572710 (associated with component A) and MGPS J164728−572544 (component B). The reported peak and integrated flux densities are 15.4±1.1 mJy beam^{-1} and 62 ± 6 mJy for the component A and 11.5 ± 1.1 mJy beam^{-1} and 34 ± 5 mJy for component B. These radio counterparts are partially resolved, as seen in Fig. 5. Component B shows a small north-east extension which does not correspond to either the optical or MIR emission. Component A peaks in the region obscured by the bright foreground star HD 150915 and also shows two fainter extensions corresponding to the emission in both the optical

and MIR (Fig. 5, left and middle). No significant radio emission at 843 MHz is observed from the inner region of the star-forming ring associated with component A. It is possible that component C also has a radio contribution hinted at by the overlaying elongated MGPS2 radio contours in this region.

The system is also detected in the Parkes-MIT-NRAO (PMN) South Survey (Wright et al. 1994) at 4.85 GHz, and catalogued as PMN J1647−5726. Because of the much poorer PMN resolution (∼4.2 arcmin), the system is only detected as an unresolved point source with a flux density of 37 ± 8 mJy, very close to the detection limit of 32 mJy. Fig. 5 (right) shows the PMN radio contours with a peak flux of 37 Jy beam^{-1}. An apparent extension to north-east, similar to the one at 0.843 GHz, is visible. Due to the large beam size of the PMN survey, it is likely that this extension is caused by the confusion with the nearby radio point source PMN J1648−5724 ∼5.5 arcmin to the north-east. This is intriguing as the MGPS2 contours at the north-east edge of component B and the south-west edge around the nominal radio point source PMN J1648−5724 are almost aligned. However, there is no evidence of an optical galaxy counterpart to this compact source.

Using the integrated flux densities at 4.8 GHz and 0.843 GHz (summed components A and B), we estimate a system-wide spectral index of $\alpha \sim -0.5$ (defined from $S_\nu \propto \nu^\alpha$). This estimate is uncertain for several reasons: (i) the accuracy of the flux density at 4.8 GHz is poor because of possible confusion with the nearby source and proximity to the sensitivity limit, (ii) the accuracy of the flux density at 0.843 GHz suffers from the measurement method (Gaussian fitting) which assumes that both radio objects are unresolved, and (iii) the estimate of the spectral index from only two points assumes that the spectral energy distribution (SED) is flat in that spectral region (e.g. the free–free emission in the $\nu < 1$ GHz region could be optically thick). However, the estimated radio SED is in agreement with SED's of normal galaxies (Condon 1992); i.e. a mixture of thermal emission originating from bright, star-forming, H II regions, and non-thermal emission from diffused, ultra-relativistic electrons and supernova remnants (SNRs).

A proper interpretation of the components's radio SED and separation of the thermal and non-thermal component (which could lead to an independent estimate of the SFR) requires new, high-resolution and high-sensitivity observations at several frequencies and in the high-frequency range (1–10 GHz).

4 FOLLOW-UP OPTICAL SPECTROSCOPY

Initial spectroscopy was obtained using the now decommissioned double beam spectrograph (DBS) on the 2.3-m MSSSO telescope in 2005 June. The four positions were centred on the brightest knots in the system and are summarized in Table 2 and shown in Fig. 6. The DBS gives two simultaneous blue and red spectra and our choice of gratings covered the range 3520–5430 Å in the blue and 5950–6900 Å in the red. The dispersion was 1 Å per pixel in the blue arm and 0.5 Å per pixel in the red arm. The 1D spectra were obtained by summing over the extent of the compact emission on the slit and were flux-calibrated following standard IRAF routines. The typical on-site seeing is 1.5–2.5 arcsec.

Additional spectroscopy was obtained using the WiFeS integral-field instrument on the 2.3-m MSSSO telescope (Dopita et al. 2010) in 2011 July. WiFeS is an 'image slicing' integral-field spectrograph made of up 25 1-arcsec-wide adjacent 'slices' on the sky each of which is 38 arcsec long. This creates an effective on-sky field of view of 25 × 38 arcsec with the long axis oriented east–west in standard configuration. The sky background was subtracted using empty

Table 2. Summary DBS and WiFeS IFU observations from 2005 June (DBS) and 2011 July (WiFeS). The DBS velocities are accurate to ∼50 km s^{-1} and WiFeS ∼20 km s^{-1}.

| Pointing	RA (J2000)	Dec. (J2000)	Instrument	Velocity (km s^{-1})
Knot I				
I.1	16:47:28.68	−57:25:34	WiFes	799
I.2	16:47:26.61	−57:25:34	WiFes	812
I.3	16:47:27.15	−57:25:29	WiFes	808
I.4	16:47:26.60	−57:25:21	WiFes	807
Knot II				
II.1	16:47:27.90	−57:25:45	DBS	803
II.1	16:47:27.90	−57:25:45	WiFes	799
II.2	16:47:28.90	−57:25:33	WiFes	800
Knot III				
III.1	16:47:25.30	−57:26:04	DBS	806
III.1	16:47:25.30	−57:26:04	WiFes	823
III.2	16:47:25.80	−57:26:15	WiFes	836
III.3	16:47:27.10	−57:26:07	WiFes	834
Knot IV				
IV.1	16:47:19.68	−57:25:51	DBS	827
IV.1	16:47:19.68	−57:25:51	WiFes	880
IV.2	16:47:21.50	−57:25:48	WiFes	864
IV.3	16:47:20.90	−57:25:49	WiFes	871
Knot V				
V.1	16:47:17.18	−57:26:07	WiFes	909
V.2	16:47:17.82	−57:26:03	WiFes	901
Knot VI				
VI.1	16:47:14.80	−57:26:23	DBS	751
Knot VII				
VII.1	16:47:15.90	−57:26:44	WiFeS	938
VII.2	16:47:18.25	−57:26:51	WiFes	910
VII.3	16:47:14.83	−57:26:48	WiFes	959
VII.4	16:47:17.55	−57:26:55	WiFes	932
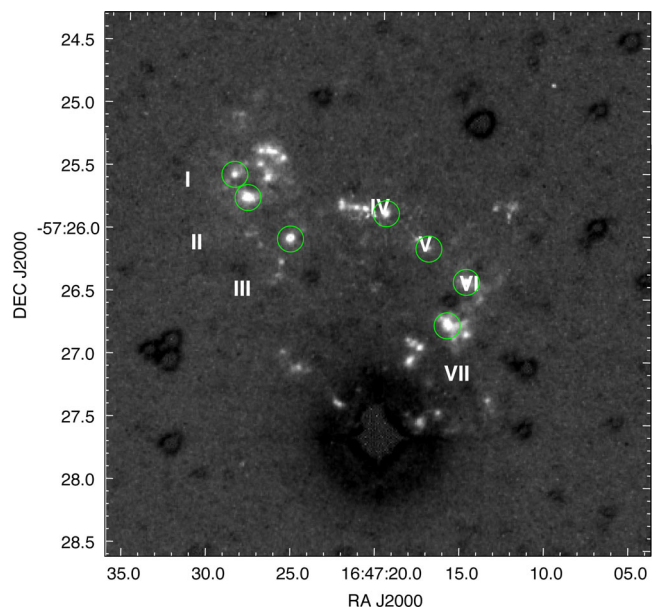
Figure 6. The locations of the spectroscopically observed emission knots given in Table 2 overlaid on the 4 × 4 arcmin SHS H α quotient image.
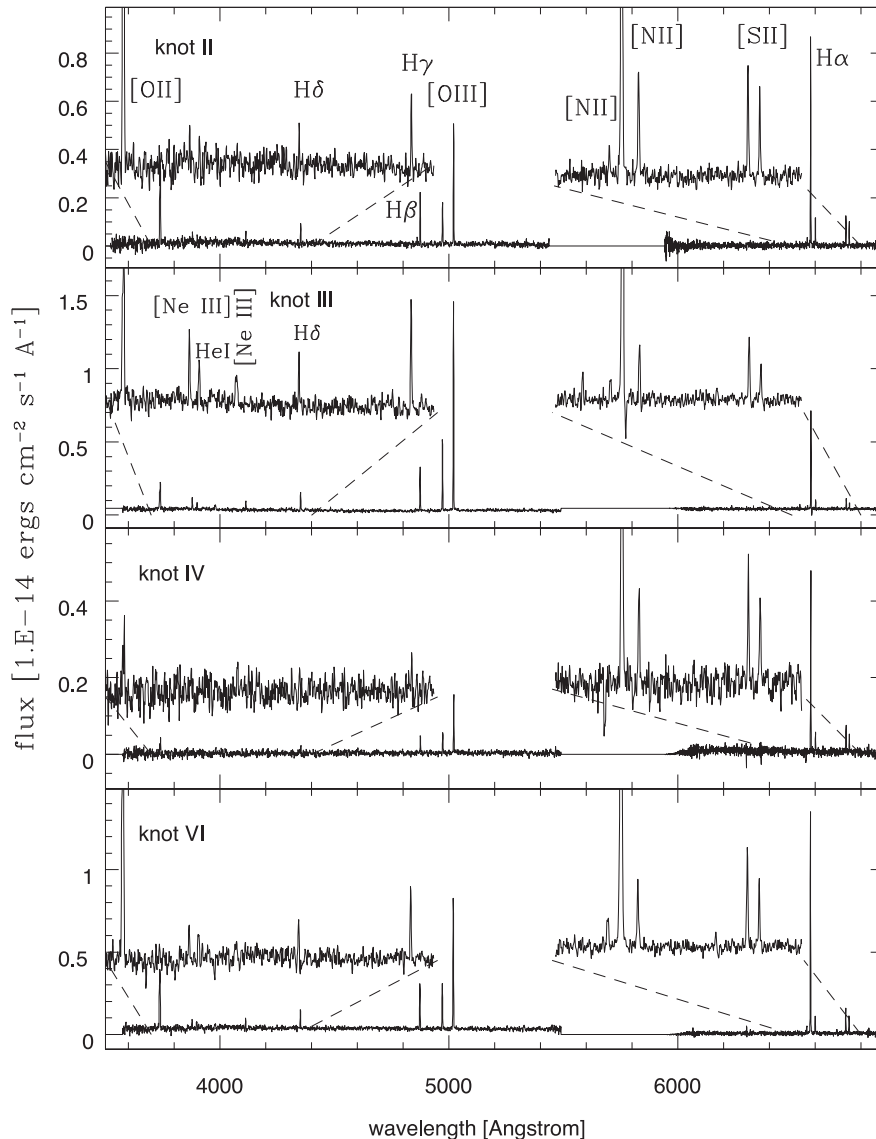
Figure 7. The four DBS spectra, numbered according to position in Table 2. Extracted spectral regions are shown enlarged to bring out fainter lines. The red and blue zoom windows show the spectral ranges 3700–4400 Å and 6500–7700 Å. The spectra are typical of H II regions with strong Balmer emission and forbidden lines of [O III] , [N II], and [S II]. Note the [Ne III] lines in the blue data of the higher S/N spectrum for knot III.

areas of the observed field or from offset sky pointings. The weather was partly cloudy and though flux calibration was performed, the atmospheric transmission changed significantly between pointings. We used the $R = 7000$ grating with coverage from 5800 Å to 7000 Å and dispersion of 0.44 Å per pixel. Only the prominent knots in each WiFeS pointing were extracted and used as the S/N in the inter-knot regions is too low (partially because of the non-optimal observing conditions) for additional useful spectra to be extracted or to create a 2D line intensity map or a reliable 2D velocity field. Deeper Integral Field Unit (IFU) observations on a larger telescope are clearly motivated.

A total of seven combined DBS and WiFeS pointings were obtained, centred on the brighter knots in the system as shown in Fig. 6, including three WiFeS repeats of some of the earlier DBS observations for consistency checks. The positions are listed in Table 2. For WiFeS, several knots can be observed simultaneously for each pointing. A spectrum through the data cube was obtained by placing apertures over each knot and wavelength sum-

ming the pixels within each aperture. A combined 1D spectrum was produced for each knot and used to derive velocities from fits to the [N II], H α, and [S II] emission lines and taking the weighted average.

Velocities to better than ~50 km s^{-1} are achievable with the DBS system and grating combination, but with some flop and flexure being an issue with this large rotating spectrograph off the Nasmyth focus (Rodgers, Conroy & Bloxham 1988). Spectral calibration errors from the red WiFeS data cube are of the order of 0.05 Å (see Childress et al. 2014) or 2.3 km s^{-1} at H α. Arc calibrations exposures were taken for each object observation to remove any effect of temperature variations inside WiFeS. This set-up enables us to resolve velocity dispersions across resolved systems down to σ ~20 km s^{-1} (Vogt et al. 2015). In our data velocity measurements of individual knots in one WiFeS pointing agree to better than 10 km s^{-1}. DBS velocities show significant scatter of 50 km s^{-1} between the blue and the red arm and are less accurate. Where the same knot is measured with both WiFeS and DBS, there

Table 3. SuperCOSMOS and Sextractor isophotal magnitude estimates for main system components. The asterisked *I*-band entry for component A came from the IAM data from the SR/H α SuperCOSMOS images and may be underestimated given the Sextractor value. Sextractor values are from Doyle et al. (2005).

Component	B_j	R1	R2	I	Origin
A	13.1	–	13.3	12.8	Sextractor
A	–	14.98	13.85	11.3*	IAM (SuperCOS)
B	–	15.61	15.26	13.86	IAM (SuperCOS)
C	–	16.27	16.26	16.0	IAM (SuperCOS)

is acceptable agreement in two cases but the offset is fairly large ($\sim$50 km s^{-1} in the third case (knot IV) and is at the upper error level that might be expected. It is clear from Fig. 7 that the spectral continuum for Knot IV is lower than for the other spectra shown.

Fig. 7 presents the 1D blue and red emission line spectra from the DBS for knots II, III, IV and V. Extracted regions are shown enlarged to show the fainter lines. The spectra are typical of H II regions and exhibit the standard emission lines of [O II] 3727 Å, the Balmer series (Hδ Hγ, Hβ) and [O III] in the blue region. In the red there is H α and the weaker bracketing [N II] lines. The [S II] doublet is also well detected and resolved providing an opportunity to estimate electron densities. These are near the low-density limit ($n_e \leq$100–200 cm^{-3}) from measurements across four knots. For knot III, which is the highest surface brightness compact emission region in the entire system, the higher S/N spectrum reveals [Ne III] lines at 3869 and 3968 Å rest wavelengths. There is no evidence for Wolf–Rayet features in any of these H II region spectra.

5 ANALYSIS

5.1 Optical photometry

Component A (the main ESO 179-13 galaxy) has optical photographic photometry in the B_J, R, and I bands (Doyle et al, 2005), while Lee et al. (2011) give $B \simeq 15$. In the broad-band SuperCOSMOS photographic data (Hambly et al. 2001a), the isophotal image parameters for component A are blended with the bright star in the B_J band, so no reliable magnitude is possible from the standard image-analysis mode (IAM) processing. This led Doyle et al. (2005) to estimate individual Sextractor magnitudes for component A when constructing optical photometry for HIPASS galaxies. These were bootstrapped to the various SuperCOSMOS zero-points for each band. However, the areal profile fitting and image deblending techniques employed by the SuperCOSMOS IAM software (Hambly et al. 2001a) do enable component magnitude estimates to be obtained. There are three R-band magnitudes available from the first and second epoch broad-band surveys and from the SR exposure taken as part of the H α survey. I-band SuperCOSMOS magnitudes are also available. For isolated sources such magnitudes are accurate to ±0.1. These results are presented in Table 3. The IAM results from components B and C are likely to be more reliable than for component A whose I-band magnitude in particular seems grossly underestimated when compared to the independent Sextractor value from Doyle et al. (2005) and the 2MASS NIR photometry for any sensible colour term. We estimate small colour terms of $I - K_s \sim$1.0 for component A and $\sim$1.4 for component B.

5.2 Infrared photometry

The available infrared photometry obtained is presented in Table 4 with data gathered from various archives including Skrutskie et al.

Table 4. Infrared photometry for the combined system unless otherwise stated. *WISE* values are aperture corrected.

λ	Band	Flux density (mJy)	(mag)
1.2 μm	2MASS *J*		9.571
1.7 μm	2MASS *H*		9.122
2.2 μm	2MASS *Ks* LGA	184	8.895
3.4 μm	*WISE* W1	129.51	8.45
4.6 μm	*WISE* W2	82.38	8.30
12 μm	*WISE* W3	269.80	5.17
22 μm	*WISE* W4	739.20	2.63
12 μm	*IRAS* 12 μm	<250	
25 μm	*IRAS* 25 μm	<295	
60 μm	*IRAS* 60 μm	3930 ± 830	
100 μm	*IRAS* 100 μm	14 200 ± 1600	
65 μm	*AKARI* FIS N60	2179 ± 748	
90 μm	*AKARI* FIS WIDE-S	4982 ± 272	
140 μm	*AKARI* FIS WIDE-L	8730 ± 1140	
160 μm	*AKARI* FIS N160	6105 ± 3460	
350 μm	*Planck* 857 GHz	7264 ± 1629	
550 μm	*Planck* 545 GHz	1512 ± 760	

(2006) for 2MASS. The integrated K_s-band photometry was obtained from the 2MASS 'Large Galaxy Atlas' (LGA; Jarrett et al. (2003). A total K_s-band magnitude of 8.95 is obtained from an aperture of 177.8 × 56.9 arcsec that combines the three systems though the contribution from component C and diffuse component is minimal. We carried out differential aperture photometry on the two main sub-systems A and B and found a K_s-band difference of 2.2 mag with component A being the brighter. We find $m_K(A) = 10.3$ mag and $m_K(B) = 12.5$ mag, for the main bodies of components A and B only (i.e. the main disc for A and the core region of B).

The system corresponds to IRAS 16430−5721 in the Point Source Catalog for the Infrared Astronomical Satellite (Beichman et al. 1988). The galaxies were detected in the 60 and 100μm bands, but only upper limits are reported in the 12 and 25μm bands.

Both the *AKARI*/Infrared camera All-Sky Survey Point Source Catalogue (Ishihara et al. 2010) and the *AKARI*/Far Infrared Surveyor (FIS) Bright Source Catalogue (Yamamura et al. 2009) also report flux densities for the objects. However, the *AKARI* 9μm detection comes from the bright star and not the galaxy. HD 150915 is a visual binary with components 10 arcsec apart. The companion star (not in SIMBAD) is redder with $(J - K_s) = 1.1$. The two stars have similar magnitude in the mid-infrared: 7.45 and 7.36 in $W2$, and 7.20 and 7.22 in $W3$. The *AKARI* 9 μm position is in between the two stars. The two stars have no infrared excess (McDonald, Zijlstra & Boyer 2012). The *AKARI* FIS measurements at 65 and 160 μm are <3σ detections.

The *Planck* Catalog of Compact Sources Release 1 (Planck collaboration XXVIII, 2014) lists flux densities at 545 and 857 GHz (550 and 350μm), although the 545 GHz measurement is only a $\sim$2σ detection. A summary of the available infrared photometry is presented in Table 4.

5.3 H I and optical spectroscopic velocities

The H I HIPASS spectrum of the system from a pointing at 16^{h}47^{m}20ˢ0, −57°27′06″ (J2000) is reproduced in Fig. 8. The 20 per cent line width is 222 km s^{-1} and these data provide a systemic heliocentric velocity of 842 km s^{-1} (Koribalski et al. 2004).
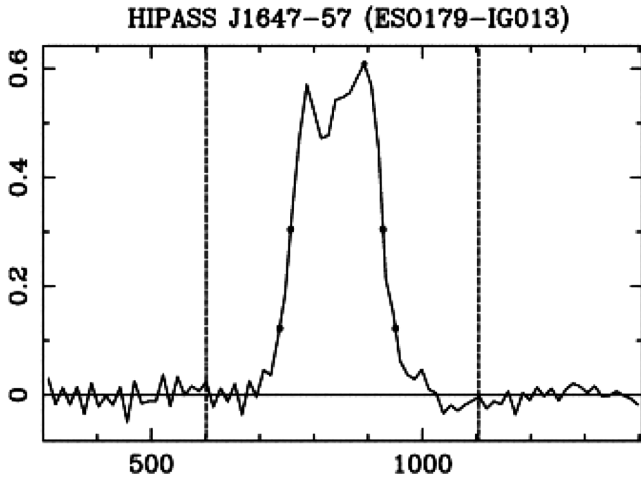
HIPASS J1647–57 (ESO179–IG013)

Figure 8. The H I spectrum from the HIPASS survey (Koribalski et al. 2004) taken from a pointing at $16^h47^m20\overset{s}{.}0$, $-57°27'06''$ (J2000). The y-axis is flux in Jy, and the x-axis heliocentric velocity in km s^{-1}. The H I velocity is 842 km s^{-1} taken at the mid-point of the H I profile at the 20 per cent level which has a velocity width of 222 km s^{-1}.
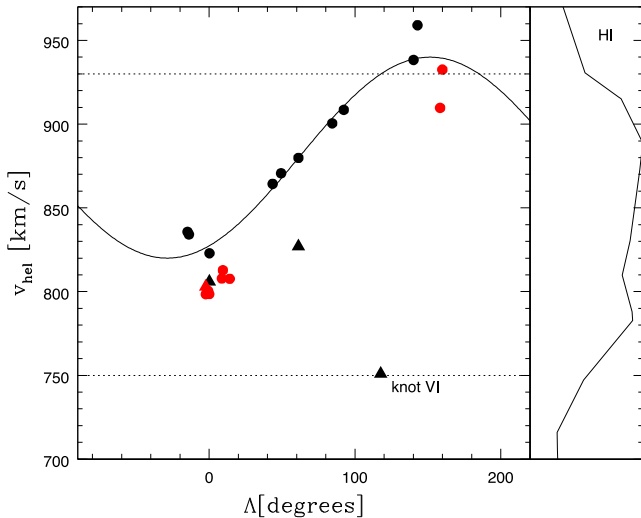

Figure 9. The distribution of velocities of the star-forming regions that are located along the ring (black) and further out or internal to the ring, including from component B and C (red). Circles are WiFeS data and triangles DBS. The horizontal axis shows the angle along the ring, starting from the direction of the assumed bullet, galaxy component B. On the right-hand side, the HIPASS spectrum has been plotted for ease of comparison.

For our optical observations, we used the WiFeS and DBS spectra to derive heliocentric velocities of several of the most prominent emission knots, using weighted averages from fits to the key emission lines. These results can be used to trace the velocity of the knots in the main ring and for the other star-forming regions in component B, but not of the central disc where there is little star formation and where we did not obtain spectra. We rely on the published results for component A.

Our new spectroscopic results are shown in Fig. 9. The vertical axis shows the heliocentric velocity of each knot. On the right-hand side of the figure, we have added the HIPASS spectrum plotted with velocity on the same scale for ease of comparison. The horizontal axis shows the angle along the ring, where a position angle of zero corresponds to the direction of component B. This is considered the

bullet because of the lack of other obvious galaxies in the broadband imaging within 30 arcmin (∼5.2 Mpc). Black symbols are knots which we consider as part of the ring as they fall along the ring's locus even if they have a discrepant velocity. Red symbols are for knots in galaxy components B or C, located inside or outside of the ring. Circles are the WiFeS data and triangles the (less accurate) DBS data. There appears to be one particularly anomalous DBS velocity for knot VI at only 750 km s^{-1}. This knot is the second most intense star-forming region in the entire system. There is no corroborating WiFeS spectrum for this knot to check the DBS result.

The velocity distribution for the knot samples around the ring shows a sinusoidal pattern as function of ring position angle, with systemic velocity of 880 km s^{-1} and an amplitude of 60 km s^{-1}. This velocity pattern can be interpreted as rotation or expansion, or a combination of both. The fact that the extrema of the velocity fall along the major axis is indicative of rotation being the dominant component. The velocity corrected for inclination of the ring gives 85 km s^{-1}. If this is rotation, the interior mass would be ∼10^{10} M$_\odot$, somewhat higher than the baryonic mass derived below for component A.

The red points at angle zero show the velocity distribution of the most conspicuous knots seen in the component B galaxy (the assumed bullet) including for knots labelled I and II in Fig. 6. The average of these is 805 km s^{-1}, with little dispersion and is separated from that of the ring at this position angle of ∼830 km s^{-1}.

5.4 Masses

5.4.1 Derived stellar mass

The system's stellar mass can be derived from the *WISE* drizzle images using the relation of Cluver et al. (2014), calibrated from the stellar masses in the Galaxy and Mass Assembly (GAMA) survey (Taylor et al. 2011). The relation is

$$\log\frac{M_*}{L_{W1}} = -2.54\,(W1 - W2) - 0.17, \tag{1}$$

where L_{W1} is the in-band luminosity, i.e., the luminosity of the source as measured relative to the Sun in the $W1$ band as defined in equation (1) in Cluver et al. (2014).

Using $L_{W1} = 8.27 \times 10^9$ L$_\odot$, we obtain a stellar mass of $M_* = 2.4 \times 10^9$ M$_\odot$ for the entire system. The colour correction used in this method aims at accounting for the contribution from a young stellar population. Without this correction, derived masses would have been a few times higher.

The stellar masses can also be estimated from their K_s-band luminosities. The K_s-band magnitudes were measured using 2MASS aperture photometry, subtracting the field stars within the aperture. The K_s-band image (Fig. 4) clearly shows the main galaxy and a weak but definite detection of galaxy component B. The starforming ring is not discernible but evidence of a faint wash of NIR flux internal to the ring is seen, as well as a weak detection interior to the south-west edge of the ring associated with component C previously identified as WKK 7457. As the K_s-band primarily shows the older stellar population, the main body of component A appears most prominent.

Using the 2MASS K_s imaging and assuming a mass-to-light ratio of 0.80 (Bell et al. 2003), we find a stellar mass of the main components of 1.29×10^9 M$_\odot$ and 1.70×10^8 M$_\odot$ for A and B, respectively. Their mass ratio is a factor of 7.5.

The integrated K_s-magnitude of 8.95 gives a total stellar mass of 4.7×10^9 M$_\odot$, in broad agreement with the *WISE* derivation. The

mass-to-light ratio at K_s varies by a factor of 2 over a wide range of stellar ages excluding the very youngest stars (Drory et al. 2004). The models of Henriques et al. (2011) show that the K_s-band can be significantly enhanced by younger, more massive, asymptotic giant branch stars, and include a component from red supergiants.

5.4.2 Gas and dust mass

The H I neutral hydrogen mass is reported by Koribalski et al. (2004) as $M_{\mathrm{H\,I}} = 2 \times 10^9 \, \mathrm{M_\odot}$. This is similar to the overall stellar mass of the entire system which is therefore gas rich. It is not clear where the bulk of the gas originates, but the large H I mass makes an original association with component A more likely.

The mass in molecular gas is not known. CO data are required to determine this directly. Stark et al. (2013), provide evaluations of molecular to neutral hydrogen (H2/H I) ratios from a broad sample of field galaxies spanning early-to-late types, evolutionary stage and stellar masses of $10^{7.2}$ to $10^{12} \, \mathrm{M_\odot}$. Their sample is not statistically representative because CO measurements for low-mass systems such as ours are lacking. It does seem that for a range in $g - r$ of ~0.3, molecular to neutral gas ratios range from 1 to ~10 per cent, so ~$10^9 \, \mathrm{M_\odot}$ in molecular hydrogen is possible.

We use two different methods to estimate dust masses using available flux estimates. The *AKARI* 65, 90, 140, and 165 μm flux densities were measured using methods optimized for unresolved sources (Yamamura et al. 2009). Since the system is larger than the *AKARI* beam, the *AKARI* measurements may miss some of the extended emission[3] and could refer mainly to component A. This could explain why the *AKARI* flux estimates are lower by a factor of 2 compared to the equivalent *IRAS* values. In Table 4, we included the *AKARI* fluxes for completeness but only use the *WISE*, *IRAS*, and *Planck* data in this analysis.

The first method used fits the infrared SED with a blackbody function multiplied by an emissivity function that scales as $\lambda^{-\beta}$. We then used the resulting temperature T in the expression:

$$M_{\mathrm{dust}} = \frac{f_\nu D^2}{\kappa_\nu B_\nu(T)}, \tag{2}$$

where f_ν is a flux density measured in a single waveband, D is the distance to the source, κ_ν is the wavelength-dependent opacity, and $B_\nu(T)$ is the blackbody function.

We perform fits to the data using $\beta = 1.5$, as found empirically by Boselli et al. (2012) using *Herschel* data, and $\beta = 2$, which corresponds to the theoretical emissivity function given by Li & Draine (2001) that is frequently used in dust mass calculations. We also use the κ_ν based on values from Li & Draine (2001) to calculate the dust mass corresponding to the modified blackbody fits with $\beta = 2$. For other β values it is common to rescale κ_ν by $(\lambda/\lambda_0)^{-\beta}$, where λ_0 is some reference wavelength where the emissivity is known. Though many authors select 250 μm as a reference wavelength, it is unclear if this is appropriate, as the choice is usually poorly justified. We only calculate dust masses for fits where $\beta = 2$, but still report the temperatures for both $\beta = 1.5$ and $\beta = 2$. The dust masses from our fits are derived from the amplitudes of the best-fitting modified blackbody functions. We use a function for κ_ν, where $\lambda_0 = 240$ μm and $\kappa_\nu(250 \text{ μm}) = 5.13 \text{ cm}^2 \text{ g}^{-1}$.

[3] Any contributions from the bright stars to the south are negligible, e.g. the SED for HD 150915 star drops by >3 orders of magnitude between 1 and 10 μm.

Fits were performed to the 100, 350, and 550 μm data that tend to originate from the coldest and most massive dust component heated by the diffuse interstellar radiation field. Emission at shorter wavelengths may come from a warmer thermal component (Bendo et al. 2006, 2012, 2015). The 100 μm emission may also originate in part or entirely from dust heated by star formation. We need the data point to constrain the Wien side of the spectral energy SED, but we are also aware that the temperature may be overestimated by our analysis and the dust mass underestimated.

We calculate the dust mass using the flux density at 350 μm, the longest wavelength at which we have a $>3\sigma$ detection. At shorter wavelengths, small uncertainties in the temperature will result in relatively large uncertainties in the dust mass. We adopt $\kappa_\nu(350 \text{ μm}) = 2.43 \text{ g cm}^{-2}$ for the opacity.

We obtain dust temperatures of 19 ± 2 K for fits with $\beta = 2$ and 23 ± 3 K for $\beta = 1.5$. The slope of the 350–550μm data is more consistent with a $\beta = 2$ emissivity function than the $\beta = 1.5$ emissivity function found by Boselli et al. (2012), but given the large uncertainty in the 550μm data, it would be difficult to rule out the possibility that β is smaller than or larger than 2. The dust mass for the fit corresponding to $\beta = 2$ is $(1.1 \pm 0.3) \times 10^7 \, \mathrm{M_\odot}$.

In the second method, we fit the model templates of Draine et al. (2007) to the data. These templates are calculated for several different environments [the Milky Way, the LMC, and the Small Magellanic Cloud (SMC)], different PAH mass fractions, and different illuminating radiation fields. Draine et al. (2007) suggest fitting SED data using the following equation which we also adopt:

$$f_\nu = A \left[(1 - \gamma) j_\nu(U_{\mathrm{MIN}}) + \gamma \, j_\nu(U_{\mathrm{MIN}}, U_{\mathrm{MAX}})\right]. \tag{3}$$

In this equation, $j_\nu(U_{\mathrm{MIN}})$ is the template for dust heated by a single radiation field U_{MIN} and is equivalent to cirrus heated by a diffuse interstellar radiation field. The quantity $j_\nu(U_{\mathrm{MIN}}, U_{\mathrm{MAX}})$ is the template for dust heated by a range of illuminating radiation fields ranging from U_{MIN} to U_{MAX}, with the relation between the amount of dust dM heated by the given radiation field in the range between U and $U + dU$ given by the equation:

$$\mathrm{d}M \propto U^{-2} \, \mathrm{d}U. \tag{4}$$

This $j_\nu(U_{\mathrm{MIN}}, U_{\mathrm{MAX}})$ effectively represents the fraction of dust heated by photodissociation regions (PDRs) in the fit, and the γ term indicates the relative fraction of dust heated by the PDRs. The A term is a constant that scales the sum of the j_ν functions (which are in units of Jy cm^2 sr^{-1} H-nucleon^{-1}) to the flux density. It is related to the dust mass by

$$M_{\mathrm{dust}} = \frac{M_{\mathrm{dust}}}{M_{\mathrm{gas}}} m_{\mathrm{p}} D^2 A, \tag{5}$$

where $M_{\mathrm{dust}}/M_{\mathrm{gas}}$ is the dust-to-gas ratio, m_{p} is the mass of the proton, and D is the distance.

As this system shares many characteristics of dwarf galaxies and Magellanic systems (including the metallicity – see below), we only fit LMC and SMC templates to the data. We use all *WISE*, *IRAS*, and *Planck* data between 12 and 550μm in the fit.

We obtained best fits using templates based on the LMC2_05 model from Draine et al. (2007). The resulting U_{MIN} and U_{MAX} were 1.5 and 10^6 times the local interstellar radiation field. The best-fitting γ was 0.024 ± 0.017. This is consistent with the majority or even all the dust mass being contained in a cirrus component. The resulting dust mass is $(1.5 \pm 0.3) \times 10^7 \, \mathrm{M_\odot}$, slightly higher than that calculated using the single modified blackbody fit. This is expected given that the Draine et al. (2007) models account for the

Table 5. Stellar, gas and dust masses, star formation rates, and specific star formation rates estimated for the full system and, in so far as is known, for the individual components. Values for component A refer to the inner region (the disc), and for the core of component B. The SSFRs for A and B assume total stellar masses of 1.3×10^9 and 1.7×10^8 M$_\odot$, respectively (refer to the text).

Parameter		Full system	Component A	Component B	Ring
M_* (K_s)	(M$_\odot$)	4.7×10^9	1.3×10^9	1.7×10^8	–
M_* (*WISE*)	(M$_\odot$)	2.4×10^9	–	–	–
$M_{\rm HI}$	(M$_\odot$)	2×10^9	–	–	–
$M_{\rm dust}$	(M$_\odot$)	1.5×10^7	–	–	–
SFR (H α)	(M$_\odot$ yr^{-1})	0.33	0.01	0.08	0.24
SFR (*WISE* 12 μm)	(M$_\odot$ yr^{-1})	0.15	–	–	–
SFR (*WISE* 22 μm)	(M$_\odot$ yr^{-1})	0.47	–	–	–
SSFR (H α)	(M$_\odot$ yr^{-1} M$_*^{-1}$)	7.0×10^{-11}	7.7×10^{-12}	4.7×10^{-10}	–

mass in warmer dust components and for the relative contributions of various thermal components of dust to the SED.

The masses are summarized in Table 5. Individual stellar masses of the two systems are ∼3 times less than that of the total system, so much of the stellar mass is located outside of the brighter regions. Deeper MIR images to find the detailed location of the remainder, either in a halo or in expelled streams, would be of interest.

The two galaxy components A and B are small systems. For comparison, the stellar mass of the LMC is $M = 2.7 \times 10^9$ M$_\odot$. Its *W1* flux is 2080 Jy (Melbourne & Boyer, 2013), which scaled to 10 Mpc gives 50 mJy, about three times fainter than Kathryn's Wheel. Component A is similar to the LMC. Component B is comparable to the SMC, which has a stellar mass of 3.1×10^8 M$_\odot$.

The system contains more gas and dust than the LMC and SMC. The LMC H I mass is only 0.48×10^9 M$_\odot$ (Staveley-Smith et al. 2003), and the SMC has an H I mass of 5.6×10^8 M$_\odot$ (Van der Marel, Kallivayalil & Besla 2009). While the stellar masses are broadly comparable, the dust mass is three times higher and the neutral gas four times higher than that of the LMC and SMC combined. We do not know with certainty which of the two components (A or B) is the origin of the gas and dust emission. The gas-to-dust ratio is ∼133, which excludes the unknown molecular mass and is therefore an upper limit. For comparison, a mean gas-to-dust ratio of 58.2 was found for 78 bright galaxies in the Herschel Virgo Cluster Survey (Davies et al. 2012). Based on their study, they suggest that a factor of ∼2.9 can be used to convert atomic gas to total gas (i.e. H I + H 2) in their survey. The value of the gas-to-dust ratio for the Milky Way is ∼143 (Draine et al. 2007), a similar value to what we derive here. Interestingly, the ratio of the extent of the star-forming regions within B to that of the ring around A is similar to the ratio of the galaxy stellar masses.

5.5 Star formation rates

SFR can be derived from different tracers (e.g. Kennicutt & Evans 2012), mostly related to the UV photons produced by young massive stars. The H α luminosity and the MIR flux tracing heated dust are independent tracers of the SFR.

5.5.1 SFR from the H α flux

The SFR from the integrated H α luminosity of the system is calculated following Kennicutt & Evans (2012), using the expression

$$\log \frac{\dot{M}_*}{\rm M_\odot\ yr^{-1}} = \log L({\rm H}\alpha) - 41.27. \qquad (6)$$

Our first estimate of the integrated H α flux (and luminosity) is derived from aperture photometry on all of the clearly identifiable knots in the CTIO continuum-subtracted H α image. These included 43 knots in the ring, 8 knots in the core of component B, and 8 knots in the region of the disc that defines component A. The resulting fluxes were converted to individual SFR for each knot.

Aperture photometry was also done on the full areas covered by each of the main system components A, B, C, and the ring. This provided a global integrated SFR as H α emission is distributed more widely around the entire region and even at low levels along the main disc of component A. The results are listed in Table 5. For component B, we measured the main body, but excluded the faint outer regions because of confusion with the ring to the south. Table 5 also lists the specific SFR (SSFR: the SFR divided by the stellar mass). For the disc system component A and for B, we used the stellar masses given in Table 5. No mass was derived for the ring. For the full system we included all the stellar mass.

The conversion factor of flux units count^{-1} was derived from the individual H II knots listed in Table 2, using a 7 arcsec aperture for each. The H α flux for these knots was measured from the calibrated WiFeS IFU data. Poor weather during the WiFeS observations resulted in a factor of 2 spread in measured conversion factors. Removing the lower values left knot systems I, II, and IV. Averaging their conversion factors yields $1.2 \pm 0.3 \times 10^{-18}$ erg cm^{-2} s^{-1} per count for the CTIO image. The photometry counts were converted to flux units, and a total flux for all components of $F({\rm H}\alpha) = 3.0 \pm 0.6 \times 10^{-12}$ erg cm^{-2} s^{-1} was obtained.

Owing to possible problems with the flux calibration, an independent measurement would be useful. Unfortunately, the system is just outside the footprint of the VST/OmegaCAM Photometric H-Alpha Survey (VPHAS+) Survey (Drew et al. 2014), and while it is imaged by the calibrated low-resolution the Southern H-Alpha Sky Survey Atlas (SHASSA) survey (Gaustad et al. 2001), the proximity of HD 150915 precludes the measurement of an accurate integrated H α flux following the recipe of Frew, Bojičić & Parker (2013). However, the SHS (Parker et al. 2005) offers an alternative approach to obtaining the integrated H α flux of the system, in order to compare with our CTIO estimate. The SHS was absolutely calibrated by Frew et al. (2014a), who showed flux measurements to 20–50 per cent accuracy were feasible for non-saturated diffuse emission regions. Using the methods discussed there, and correcting for reduced transmission due to the systemic velocity, we determine an integrated H α flux of $1.1 \pm 0.5 \times 10^{-12}$ erg cm^{-2} s^{-1} for component B through an aperture of 90 arcsec; a correction for [N II] contamination is unnecessary based on the high excitation and low metallicity of the system's

H II regions. This agrees with an equivalent CTIO measurement to within the uncertainties, so we average the results to get a total flux for component B. Unfortunately the proximity of the bright star precludes an accurate flux measurement from the SHS for the star-forming ring. An approximate lower limit, based on a simple curve-of-growth analysis of several apertures is $F(H \alpha) = \sim 1 \times 10^{-12}$ erg cm^{-2} s^{-1}, also in agreement with the CTIO measurement. The total H α flux for the system, now using the weighted average of the independent CTIO and SHS calibrations, is $2.9 \pm 0.3 \times 10^{-12}$ erg cm^{-2} s^{-1}, adopted hereafter.

The systemic flux, now corrected for a reddening $E(B - V) = 0.24$ mag, and applying a Howarth ([1983](#)) reddening law, is $F_0(H \alpha) = 5.1 \times 10^{-12}$ erg cm^{-2} s^{-1}. This leads to a total luminosity, $L(H\alpha) = 6.1 \times 10^{40}$ erg s^{-1}, and a total ionizing flux, $Q = 4.4 \times 10^{52}$ photons s^{-1}, for a distance of 10 Mpc. The integrated SFR was then found to be 0.33 ± 0.09 M$_\odot$ yr^{-1} following equation (6). This SFR is about 60 per cent higher than that of the LMC, adopting the H α luminosity for the LMC from Kennicutt et al. ([1995](#)). Our estimate may be an underestimate as we have not corrected for any local extinction, though the extinction derived from the mean Balmer decrement of the brightest H II regions from our spectra is consistent with the Schlafly & Finkbeiner ([2011](#)) extinction, indicating that the internal reddening is, in at least the most luminous H II regions, minimal. There may also be photon leakage from the larger H II regions in the system as noted by Relaño et al. ([2012](#)), which might help to explain the difference between the SFRs derived from H α and 22 μm *WISE* flux (see below).

We note that the most luminous H II region complex in ESO 179-13 is centred on knot VII, with $L(H\alpha) \simeq 5 \times 10^{39}$ erg s^{-1}. This luminosity is comparable to supergiant H II regions like 30 Doradus in the LMC and NGC 604 in M 33 (Kennicutt [1984](#)). Knot VII is within component C which contains old stars as it is detected in the 2MASS imagery as a separate object. It also lies interior to the fitted ring and has a different velocity distribution to the components along the ring, exhibiting the largest velocities across the system. We still consider it likely to be a separate star-forming dwarf galaxy but further observations are required to establish this clearly and to study the relationship between components A and C.

5.5.2 SFR from the MIR flux

The warm dust continuum is best traced by the 22 μm *WISE* flux. Cluver et al. ([2014](#)) have calibrated the relation of this flux against H α-derived SFRs (corrected for extinction) from the GAMA Survey (Gunawardhana et al. 2013) and find

$$\log \frac{\dot{M}_*}{M_\odot \, yr^{-1}} = 0.82 \log \nu L(22 \, \mu m [L_\odot]) - 7.3. \tag{7}$$

This yields an integrated SFR of 0.47 M$_\odot$ yr^{-1} for ESO 179-13, somewhat higher than that derived from the de-reddened H α flux. In contrast, the 12 μm emission (Cluver et al. [2014](#)), calibrated in the same way, corresponds to a lower SFR of 0.15 M$_\odot$ yr^{-1}. The lower mass measured in the 12 μm band may be because this band detects significant PAH emission. This is relatively weak in low metallicity environments (e.g. Engelbracht et al. [2005](#), [2008](#)), so emission from bands that contain PAH emission and the SFRs based on these bands may be underestimated. All in all, the various estimates are in reasonable agreement, and we conclude that the integrated SFR is approximately 0.2–0.5 M$_\odot$ yr^{-1}.
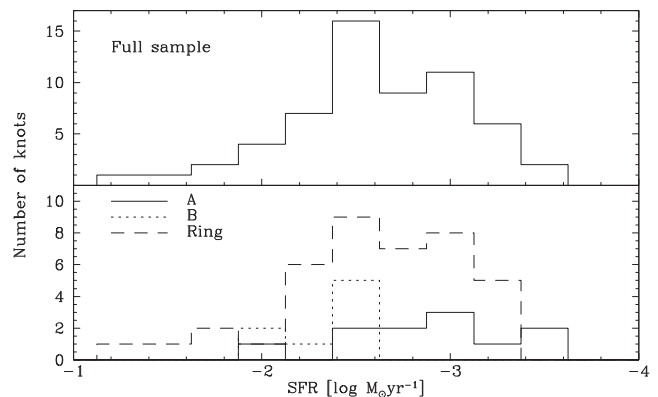

Figure 10. The distribution of star formation rates within the knots, for component A (along the disc), component B (the assumed 'bullet'), and the ring. The top panel shows the combined distribution.

5.5.3 Star formation distribution

We find that almost all of the SFR in component A (the main disc or bar) is accounted for by the main identified knots. In contrast, only 28 per cent of the SFR in component B appears concentrated in the main knots. About 44 per cent of the SFR in the main ring is incorporated in the most intense and well-defined knots. The remainder may be located in knots below the confusion limit of the available images.

The SFR in the galactic disc that comprises component A is almost entirely due to the bright region towards the south west, located on the edge of the main disc and interior to the fitted oval of the main ring shown in Fig. [2](#). There are a few further small, faint, reddened knots in the central regions but the remainder of the galaxy seems dormant. The star formation in component B is mainly concentrated in an oval region that is 30×20 arcsec in size that overlaps with the underlying galaxy detected in the optical broad-band colours and 2MASS as galaxy component B. However, there is star formation throughout a region 30–40 arcsec in radius centred on B with one small isolated blob even located 60 arcsec from the core to the north-west. There is clearly a continuum of star formation over much of the entire area where that associated with component B blends in to the north-east edge of the ring.

The distribution of SFR over the detected knots is shown in Fig. [10](#). The top panel shows the sum of the knots in components A, B and the ring, and the bottom panel shows the individual components. The brightest knot in the ring (III.1) has an SFR of 0.06 M$_\odot$ yr^{-1}. Galaxy component B lacks the tail to low SFR seen in the knots of component A and in the ring: this is likely due to the confusion limit being much brighter for B. The two strongest regions of SFR are in the ring.

5.5.4 Star-forming versus non-star-forming galaxies

Schiminovich et al. ([2007](#)) have shown that galaxies distribute over two clear sequences when the total stellar mass is plotted against SSFR. The approximate location of the sequences is shown in Fig. [11](#); the dashed lines show the 1-σ spread of the distribution. We plot the locations of component A, component B, and the total system. The SSFRs are taken from Table [5](#).

Component B falls on the star-forming sequence while component A fits close to the non-star-forming galaxies as expected from a naive view of their star-forming activity evident in the imagery. Component A would be seen as quiescent if it were not for the bright
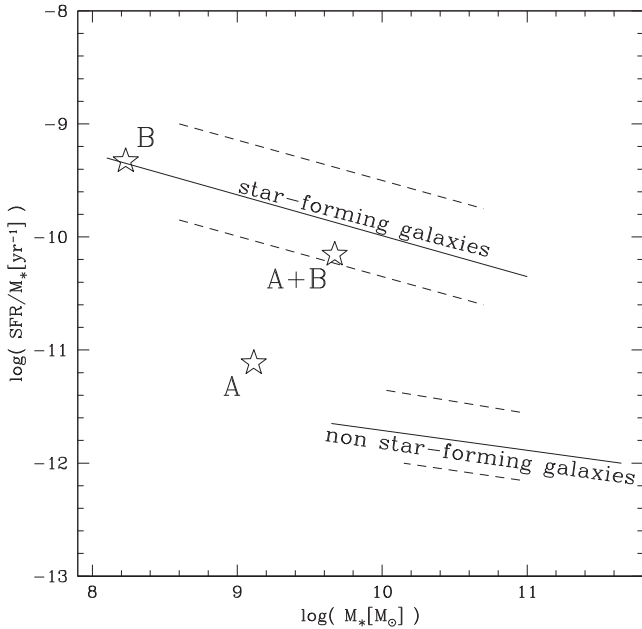
Figure 11. The distribution of star-forming and non-star-forming galaxies in the stellar mass versus specific star formation plot from Schiminovich, Wyder & Martin (2007) and adapted by Kennicutt & Evans (2012). Squares show locations of galaxies A, B and the full system. The ring is not included in the SFR for component A but is in the full system.

Figure 12. Line ratios plotted for H ɪɪ regions in several galaxies: Milky Way (filled black squares), M 31 (filled red squares), M 33 (open red squares), LMC (filled blue squares), other LG dwarf galaxies (open blue squares). Refer to the text for further details. The ESO 179-13 emission knots are shown by the large green diamonds.

region of star formation at the south-west edge of the disc. The SSFR may be underestimated if extinction is significant. Combining the entire system and using the full stellar mass and including the ring gives a data point at the lower end of the star-forming sequence. The combined system is not vigorous, even though individual components in the system are.

5.6 Abundances

The observed optical emission-line spectra of the knots can be used to derive an approximate metallicity, using the oxygen abundance as a proxy. The weakness of the [N ɪɪ] lines flanking H α in each spectrum indicates low metallicity. Modelling of the spectra is made difficult by the lack of the [O ɪɪɪ] 4363 Å line which is the main electron temperature indicator. However, metallicities can also be approximated from the [N ɪɪ] and [S ɪɪ] lines which are well detected. Fig. 12 plots the line intensities relative to H α of [N ɪɪ] and [S ɪɪ], where [N ɪɪ] refers to the 6584 Å line (the brightest of the doublet), while [S ɪɪ] refers to the sum of both the 6713 Å and 6731 Å lines. This plot, like the commonly used 'BPT' diagram (Baldwin, Phillips & Terlevich 1981), is used as a diagnostic to separate different types of emission-line nebulae, but Viironen et al. (2007) and Frew & Parker (2010) have recently shown its sensitivity as a metallicity and ionization parameter diagnostic. This diagram also circumvents the use of the [O ɪɪɪ] line which is not always detected, and uses a small wavelength range in the red which improves the relative line-to-line calibration and extinction estimates. The [N ɪɪ] and [S ɪɪ] lines are also produced at similar temperatures, alleviating the sensitivity of the collisional forbidden lines to metallicity. The plotted diagnostic is a combination of the 'N2' and 'S2' indicators of Pilyugin, Vilchez & Thuan (2010).

Fig. 12 shows the location of spectral line ratios from H ɪɪ regions measured across a variety of galaxies, in order of decreasing metallicity: M 31, the Milky Way, M 33, the LMC, and lower metal-
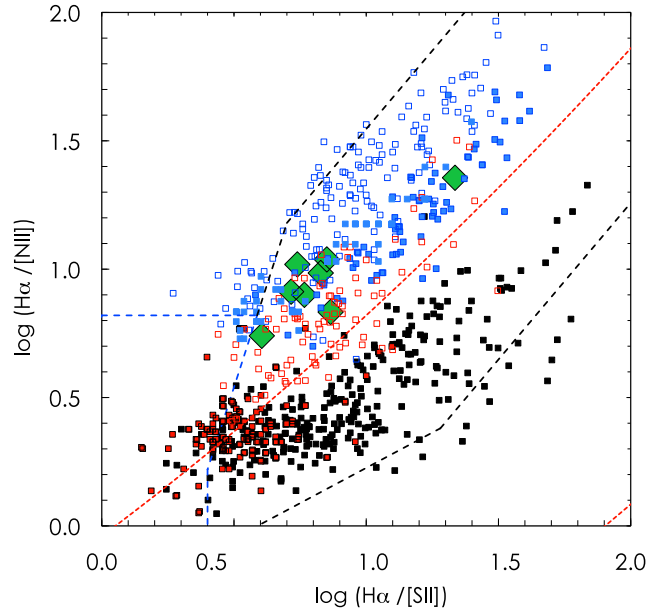
licity dwarf systems in the Local Group. The data are taken from Viironen et al. (2007, and references therein) and Frew et al. (in preparation). The boundary lines are adopted from Frew & Parker (2010) and Frew et al. (2014b), with the black-dashed trapezoid showing the domain of H ɪɪ regions. The plot shows a clear trend with metallicity with the different systems being well separated. Note that red curves enclose the planetary nebula domain (generally of higher excitation) and the blue-dash enclosed area at the lower left is occupied by shock-excited SNRs (Sabin et al. 2013). The filled green diamonds show the location of the individual knots measured in ESO 179-13. Their location in the plot coincides well with H ɪɪ regions in the LMC, and therefore the galaxies can be considered to have a similar metallicity. Indeed, the relations of Pilyugin et al. (2010) indicate a metallicity of [O/H] $\simeq$ −0.4 for ESO 179-13, consistent with a value for the LMC. This makes it likely that the majority of the gas feeding the knots originated from galaxy A, which has a similar total mass and luminosity to the LMC. Component B has a mass similar to the SMC and may therefore be expected to have a lower metallicity and gas content.

5.7 Ages

When did the bull's-eye encounter occur between galaxies A and B? An age estimate can be derived from the projected angular separation between the two components of 3.9 kpc and the observed heliocentric velocity difference between them. We assume they are effectively at the same distance and that the observed difference in the heliocentric velocities is due to their peculiar motions and that there is no relative acceleration. No transverse velocity component can be obtained so the estimated age is a lower limit. We use the average of the three literature values for component A from Strauss et al. (1992), Di Nella et al. (1997), and Woudt et al. (1999) of 761 km s^{-1} together with our newly determined value for component B from the average of several prominent emission knots in the system which gives a velocity of 806 ± 32 km s^{-1} from fits to 13

emission lines across the blue and red spectral regions. There is a nominal 45 km s^{-1} difference which produces an encounter age of 87 million years. If we assume the transverse velocity is of the same order as that along the line of sight then this introduces a root 2 factor leading to a revised age of 123 million years. System age can also be estimated from the expansion assumed for the ring. Using an assumed inclination of 45 °, and a velocity amplitude (de-projected rotational/expansion velocity) of 85 km s^{-1} then an age of 30 Myr is obtained. This is a lower limit as the velocities are mostly due to rotation, and the above assumes all is expansion.

6 DISCUSSION

6.1 Dwarf rings

ESO 179-13 is among the smallest collisional ring galaxies known. The ring diameter of 6.2 kpc is the smallest of the Madore et al. (2009) catalogue, where diameters range up to 70 kpc. Components A and B are separated by only 4 kpc, while in the full catalogue, the colliding components are almost always more than 10 kpc apart (Conn et al. 2011). The absolute K-band magnitude of ESO 179-13 is $M_K = -21.1$. Madore et al. (2009) list only 10 objects that are less luminous.

Because ESO 179-13 shows a full ring, it is a unique case of a dwarf cartwheel-type galaxy. It is more than 1.5 mag (a factor of 4) fainter than the next faintest example, Arp 147 ($M_K = -22.8$ mag). It shows that the process causing full rings can also act in interacting dwarf galaxies. Such galaxies have smaller cross-sections and shorter dynamical time-scales, which may make such occurrences less frequent, but does not stop ring formation altogether.

The difference in K-band magnitude between components A and B is 2.2 mag. This is at the very top end of the distribution in Madore et al. (2009). As component A is already one of the smallest galaxies in the Madore et al. sample, component B is possibly the smallest of all known bullet galaxies causing (partial) rings. The mass ratio between A and B may be close to the limit for the formation for collisional rings formation (D'Onghia, Mapelli & Moore 2008).

6.2 Environment

Collisional ring galaxies tend to be found in low-density environments and avoid dense clusters (Madore et al. 2009). ESO 197-13 is also seen to be in a region devoid of major galaxies. The SHS images show no Hα-emitting companions within a degree of ESO 179-13. The broad-band SuperCOSMOS R-band data reveal no other obvious galaxy of any kind within half a degree of the centre of Kathryn's wheel. There is a HIPASS galaxy with an almost identical velocity 1°.5 away: J1636-57 but is much fainter, with an integrated flux of 2.8 Jy.km s^{-1}. Given the similarity in velocity and the angular separation of 260 kpc, a physical association is possible. Galaxy J1620-60 also has the same velocity, is a few times fainter (37.4 Jy.km s^{-1}) than ESO 179-13, but is over seven degrees, over 1 Mpc, away. The nearest large galaxy is NGC 6744, a grand-design barred spiral (Ryder, Walsh & Malin 1999). It has an identical velocity and assumed distance (Kankare et al. 2014) and a projected separation of 19°.1, or 3.2 Mpc from ESO 179-13. It is unlikely to have interacted with this system.

6.3 Impact parameter

The ring's centre is displaced from that of component A by about 580 pc. We take this as the impact parameter of the collision with the bullet component B. The chances of a random (first) encounter between two isolated systems so close to the centre of A seems remote. Assuming three galaxies within a sphere of 250 kpc radius, and a relative velocity of 100 km s^{-1}, the chance of such a close encounter within a Hubble time is approximately 10^{-4}. Assuming 2×10^5 galaxies within 10 Mpc, the chance of one such a close encounter happening within 10 Mpc within the past 10^8 yr (the lifetime of the ring) is 15 per cent. This calculation suggests that ESO 197-13 is likely the closest collisional ring galaxy to the Milky Way.

The calculation ignores gravitational focusing. The gravity of the main galaxy bends the trajectory of the bullet towards it, increasing its capture cross-section. This decreases the resultant impact parameter b. For $v = 100 \, \mathrm{km \, s^{-1}}$ and $M = 6.6 \times 10^9 \, \mathrm{M_\odot}$, the reduction is given by

$$\frac{b}{b_0} = \sqrt{\left(1 + \frac{2 \, G M}{b v_0^2}\right)^{-1}} \approx 0.7. \tag{8}$$

This doubles the chances to 30 per cent, and suggests a space density of $7 \times 10^{-5} \, \mathrm{Mpc^{-3}}$. This estimate shows that the existence of one such system within 10 Mpc is quite plausible.

6.4 Lessons and prospects

The discovery of Kathryn's Wheel shows that the processes forming full rings can act in Magellanic-type systems. Full rings have only been seen and studied in large, spiral galaxies, and so their formation has been assumed to require systems with halo masses above $5 \times 10^{11} \, \mathrm{M_\odot}$ (e.g. D'Onghia et al. 2008) though the catalogue of Madore et al. (2009) does seem to extend to a few galaxies as small as ESO 197-13. As dwarf galaxies outnumber other Hubble types by a factor of ~1.4 (Driver 1999), dwarf collisional rings may also outnumber those systems involving spiral galaxies. This is shown by the space density derived above: it is 10 times higher than that of Few & Madore (1986), whose numbers are derived from more luminous galaxies.

Both components appear to have been gas-rich prior to collision. We assume the ring is formed in gas associated with component A, and so was gas-rich even though it shows little star formation now (as is normal for residual galaxies within collisional ring systems). The collision may have diverted its gas out of the main disc. It is noteworthy that component B shows vigorous star formation and may show its own (small) ring. It survived the encounter much better than A whose future evolution will be dictated by the depletion of its original gas reservoir even if the underlying stellar population seems largely unperturbed. Arp 147 is another case where both colliding galaxies formed rings though they are very different in nature. Table 6 gives a summary table of the remaining key system parameters previously available or newly compiled.

'Kathryn's Wheel' is an important system that can be used to study collisional rings as it is much closer than any equivalent, opening new possibilities for analysis. System dynamics can be studied at unprecedented spatial resolution as 0.1 arcsec (e.g. *Hubble Space Telescope* and/or AO resolution) is only 25 pc. This is sufficient to explore details of the system-wide star formation process and to allow detection of individual stars. It would be a prime candidate to measure the star formation history in the regions recently traversed by the ring.

Table 6. Summary table of key parameters previously available and newly derived for Kathryn's Wheel and environs.

Velocity H I (helio) (km s^{-1})	842 ± 5
Velocity (gal-centric) (km s^{-1})	736 ± 6
Velocity (Local Group) (km s^{-1})	678 ± 11
Distance (LG) (Mpc)	10.0 ± 0.7
Max. system extent (arcsec)	318×198
Max. system extent (kpc)	15.4×9.6
System metallicity [O/H]	~ -0.4
System age (Myr)	30–120
Space density (Mpc^{-3})	7×10^{-5}

7 SUMMARY

During visual scans of the SHS (Parker et al. 2005), a spectacular new collisional ring galaxy (or Cartwheel analogue) has been found, ESO 179-13, which we have named Kathryn's Wheel. With an estimated distance of only 10.0 Mpc, it is in the local supercluster but has been previously missed due its location near the Galactic plane and its projected proximity to a bright 7.7-mag star which interferes with observation.

The velocity range of all optical emission components from the main ring, component B, and the published velocity for component A is about 200 km s^{-1}. This is completely encapsulated within the full width at half-maximum of 222 km s^{-1} reported for the H I profile at the 20 per cent level centred at a heliocentric velocity of 842 km s^{-1}, which we consider representative of the overall interacting system.

At a distance of 10 Mpc, the system has an overall physical size of $\sim$15 kpc for all major components and the diffuse surrounding envelope, a total mass of $M_* = 6.7 \times 10^9$ M$_\odot$ (stars + H I) and a metallicity of [O/H]$\sim$ -0.4, that classifies it as a Magellanic-type system. It has a large reservoir of neutral gas and is the 60th brightest galaxy in the HIPASS H I survey. By some margin it is also the nearest ring system known. This system offers an unprecedented opportunity to undertake detailed studies of this rare phenomenon, where two reasonably well-matched galaxies have an encounter centred closely on the potential well of the target, larger galaxy.

REFERENCES

Amram P., Mended de Oliveira C., Boulesteix J., Balkowski C., 1998, A&A, 330, 881
Appleton P. N., Struck-Marcell C., 1996, Fundam. Cosm. Phys., 16, 111
Arp H. C., 1966, ApJ, 140, 1617
Arp H. C., Madore B., 1987, A Catalogue of Southern Peculiar Galaxies and Associations. Cambridge Univ. Press, New York
Baldwin J. A., Phillips M. M., Terlevich R., 1981, PASP, 93, 5
Barnes J. E., Hernquist L., 1992, ARA&A, 30, 705
Beichman C. A., Neugebauer G., Habing H. J., Clegg P. E., Chester T. J., 1988, The Infrared Astronomical Satellite (*IRAS*) Catalogs and Atlases. Volume 1: Explanatory Supplement, Scientific and Technical Information Division, NASA
Bell E. F., McIntosh D. H., Katz N., Weinberg M. D., 2003, ApJS, 149, 289
Bendo G. J. et al., 2006, ApJ, 652, 283
Bendo G. J. et al., 2012, MNRAS, 419, 1833
Bendo G. J. et al., 2015, MNRAS, 448, 135
Bianchi L., 2014, Ap&SS, 354, 103
Block D. L. et al., 2006, Nature, 443, 832
Boselli A. et al., 2012, A&A, 540, 54
Boselli A., Fossati M., Gavazzi G., Ciesla L., Buat V., Boissier S., Hughes T., 2015, A&A, 579, 102
Brosch N., Vaisanen P., Kniazev A. Y., Moisav A., 2015, MNRAS, 451, 4114
Burbidge E. M., Burbidge G. R., Prendergast K. H., 1964, ApJ, 140, 1617
Buta R., 1995, ApJS, 96, 39
Childress M. J., Vogt F. P. A., Nielsen J., Sharp R. G., 2014, Ap&SS, 349, 617
Cluver M. et al., 2014, ApJ, 782, 90
Condon J. J., 1992, ARA&A, 30, 575
Conn B. C., Pasquali A., Pompei E., Lane R. R., Chene A.-N., Smith R., Lewis G. F., 2011, ApJ, 741, 80
Corwin H. G., de Vaucouleurs A., de Vaucouleurs G., 1985, Univ. Tex. Monogr. Astron., 4, 1
D'Onghia E., Mapelli M., Moore B., 2008, MNRAS, 389, 1275
Davies J. I. et al., 2012, MNRAS, 419, 3505
de Vaucouleurs G., de Vaucouleurs A., Corwin H. G., Buta R. J., Paturel G., Fouque P., 1991, Third Reference Catalogue of Bright Galaxies, Volume III. Springer, New York
Dennefeld M., Lausten S., Materne J., 1979, A&A, 74, 123
di Nella H., Couch W. J., Parker Q. A., Paturel G., 1997, MNRAS, 287, 472
Dopita M. et al., 2010, Ap&SS, 327, 245
Doyle M. T. et al., 2005, MNRAS, 361, 34
Draine B. T. et al., 2007, ApJ, 663, 866
Drew J. E. et al., 2014, MNRAS, 440, 2036
Driver S. P., 1999, ApJ, 526, L69
Drory N., Bender R., Feulner G., Hopp U., Maraston C., Snigula J., Hill G. J., 2004, ApJ, 608, 742
Engelbracht C. et al., 2005, ApJ, 628, L29
Engelbracht C. et al., 2008, ApJ, 678, 804
Few J. M. A., Madore B. F., 1986, MNRAS, 222, 673
Fosbury R. A. E., Hawarden T. G., 1977, MNRAS, 178, 473
Freeman K. C., de Vaucouleurs G., 1974, ApJ, 194, 569
Frew D. J., Parker Q. A., 2010, Publ. Astron. Soc. Aust., 27, 129
Frew D. J., Bojičić I. S., Parker Q. A., 2013, MNRAS, 431, 2
Frew D. J., Bojičić I. S., Parker Q. A., Pierce M. J., Gunawardhana M. L. P., Reid W. A., 2014a, MNRAS, 440, 1080
Frew D. J. et al., 2014b, MNRAS, 440, 1345
Gaustad J. E., McCullough P. R., Rosing W., Van Buren D., 2001, PASP, 113, 1326
Gerber R. A., Lamb S. A., Balsara D. S., 1992, ApJ, 399, L51
Gil de Paz A., Madore B. F., Pevunova O., 2003, ApJS, 147, 29
Graham J., 1974, Observatory, 94, 290
Gunawardhana M. L. P. et al., 2013, MNRAS, 433, 2764
Hambly N. C. et al., 2001a, MNRAS, 326, 1279
Henriques B., Maraston C., Monaco P., Fontanot F., Menci N., De Lucia G., Tonini C., 2011, MNRAS, 415, 357

Higdon J. L., Higdon S. J. U., Rand R. J., 2011, ApJ, 739, 97

Hinshaw G. et al., 2013, ApJS, 208, 19

Howarth I., 1983, MNRAS, 203, 301

Ishihara D. et al., 2010, A&A, 514, 1

James P. A. et al., 2004, A&A, 414, 23

Jarrett T. H., Chester T., Cutri R., Schneider S. E., Huchra J. P., 2003, AJ, 125, 525

Jarrett T. H. et al., 2012, AJ, 144, 68

Kankare E. et al., 2014, A&A, 572, A75

Kennicutt R. C., 1984, ApJ, 287, 116

Kennicutt R. C., Evans N. J., 2012, ARA&A, 50, 531

Kennicutt R. C., Bresolin F., Bomans D. J., Bothun G. D., Thompson I. B., 1995, AJ, 109, 594

Kennicutt R. C., Lee J. C., Funes S. J., José G., Sakai S., Akiyama S., 2008, ApJS, 178, 247

Koribalski B. S. et al., 2004, AJ, 1, 16

Lauberts A., 1982, ESO/Uppsala Survey of the ESO(B) Atlas. European Southern Observatory, Garching

Laustsen S., Madsen C., West R. M., 1987, Exploring the Southern Sky. European Southern Observatory, Garching

Lee J. C. et al., 2011, ApJS, 192, 33

Li A., Draine B. T., 2001, ApJ, 554, 778

Lindsay E. M., Shapley H., 1960, Observatory, 80, 223

Longmore A. J. et al., 1982, MNRAS, 200, 325

Madore B. F., Nelson E., Petrillo K., 2009, ApJS, 181, 572

Marston A. P., Appleton P. N., 1995, AJ, 109, 1002

Masci F., 2013, Astrophysics Source Code Library, record ascl:1302.010

Masci F. J., Fowler J. W., 2009, in David A. B., Daniel D., Patrick D., ASP Conf. Ser. Vol. 411, Astronomical Data Analysis Software and Systems XVIII. Astron. Soc. Pac., San Francisco, p. 67

McDonald I., Zijlstra A. A., Boyer M. L., 2012, MNRAS, 427, 343

Melbourne J., Boyer M. L., 2013, ApJ, 764, 30

Meyer M. J. et al., 2004, MNRAS, 350, 1195

Murphy T., Mauch T., Green A., Hunstead R. W., Piestrzynska B., Kels A. P., Sztajer P., 2007, MNRAS, 382, 382

Parker Q. A., Bland-Hawthorn J., 1998, Publ. Astron. Soc. Aust., 15, 33

Parker Q. A. et al., 2005, MNRAS, 362, 689

Parker Q. A. et al., 2006, MNRAS, 372, 79

Pilyugin L. S., Vilchez J. M., Thuan T. X., 2010, ApJ 720, 1738

Planck Collaboration XXVIII, 2014, A&A, 571, 28

Relaño M., Kennicutt R. C., Eldridge J. J., Lee J. C., Verley S., 2012, MNRAS, 423, 2933

Rodgers A. W., Conroy P., Bloxham G., 1988, PASP, 100, 626

Romano R., Mayya Y. D., Vorobyov E. I., 2008, AJ, 136, 1259

Ryder S. D., Walsh W., Malin D., 1999, Publ. Astron. Soc. Aust., 16, 84

Sabin L. et al., 2013, MNRAS, 431, 279

Schiminovich D., Wyder T. K., Martin D., 2007, ApJS, 173, 315

Schlafly E. F., Finkbeiner D. P., 2011, ApJ, 737, 103

Schröder A., Kraan-Korteweg R. C., Henning P. A., 2009, A&A, 505, 1049

Sersic J. L., 1974, Ap&SS, 28, 365

Skrutskie M. F. et al., 2006, AJ, 131, 1163

Smith R. T., 1941, PASP, 53, 187

Smith R., Lane R. R., Conn B. C., Fellhauer M., 2012, MNRAS, 423, 543

Stark D. V., Kannappan S. J., Wei L. H., Baker A. J., Leroy A. K., Eckert K. D., Vogel S. N., 2013, ApJ, 769, 82

Staveley-Smith L., Kim S., Calabretta M. R., Haynes R. F., Kesteven M. J., 2003, MNRAS, 339, 87

Strauss M. A., Huchra J. P., David M., Yahil A., Fisher K. B., Tonry J., 1992, ApJS, 92, 29

Taylor E. N. et al., 2011, MNRAS, 418, 1587

Theys J. C., Spiegel E. A., 1976, ApJ, 208, 650

Theys J. C., Spiegel E. A., 1977, ApJ, 212, 616

Tully R. B., 1988, Nearby Galaxies Catalog. Cambridge Univ. Press, Cambridge

van der Marel R., Kallivayalil N., Besla G., 2009, in van Loon J. T., Oliveira J. M., eds, Proc. IAU Symp. 256, The Magellanic System: Stars, Gas, and Galaxies. Cambridge Univ. Press, Cambridge, p 81

Viironen K., Delgado-Inglada G., Mampaso A., Magrini L., Corradi R. L. M., 2007, MNRAS, 381, 1719

Vogt F. P. A., Dopita M. A., Borthakur S., Verdes-Montenegro L., Heckman T. M., Yun M. S., Chambers K. C., 2015, MNRAS, 450, 2593

Woudt P. A., Kraan-Korteweg R. C., Fairall A. P., 1999, A&A, 352, 39

Woudt P. A., Kraan-Korteweg R. C., 2001, A&A, 380, 441

Wright A. E., Griffith M. R., Burke B. F., Ekers R. D., 1994, ApJS, 91, 111

Wright E. l. et al., 2010, AJ, 140, 1868

Yamamura I. et al., 2009, in Takashi O., Glenn J. W., Takao N.Issei Y., ASP Conf. Ser. Vol. 418, AKARI, a Light to Illuminate the Misty Universe. Astron. Soc. Pac., San Francisco, p. 3

Zwicky F., 1941, in Theodore von Kármán Anniversary Volume: Contributions to Applied Mechanics and Related Subjects. California Institute of Technology, Pasadena. p. 137

This paper has been typeset from a TEX/LATEX file prepared by the author.